Aerated Flow Measurement and Modelling of a Coriolis Flowmeter

Thermal Energy and Process Engineering

Master Thesis written by Katrine Arnoldsen Juhl

June 2014

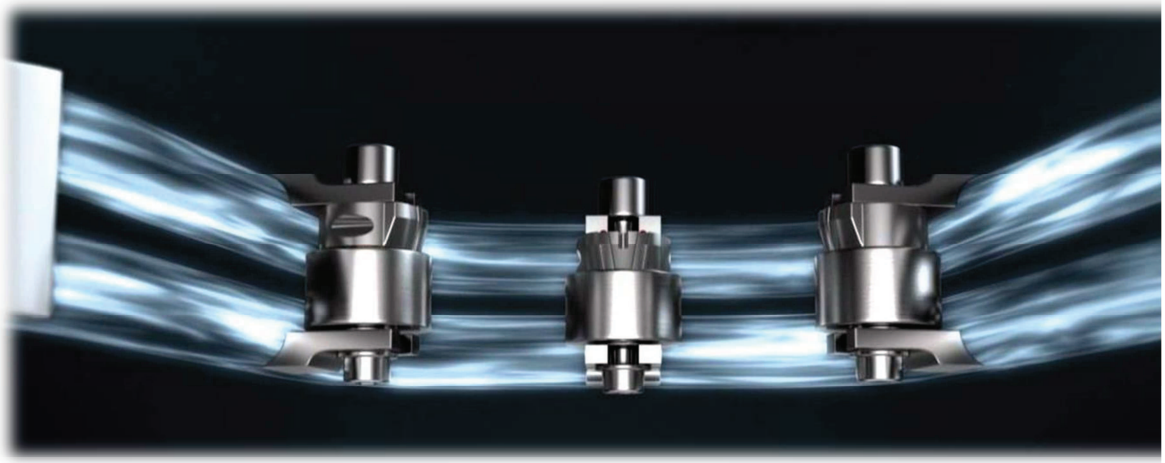

AALBORG UNIVERSITY
STUDENT REPORT

Aalborg University
School of Engineering and Science
Department of Energy Technology

Abstract

The purpose of this project was; to investigate the influence of aerated flow in a Coriolis flowmeter based on experiments of two different Coriolis flowmeters, to perform Computational Fluid Dynamics, CFD simulations of the fluid behaviour in a SITRANS FC400 sensor to the Coriolis flowmeter and to achieve an understanding of the theories applied in two-phase flow.

The theory of how the Coriolis flowmeter works was explained through the means of Coriolis forces, beam theory and phase-shift graph. For describing the fundamental theory of two-phase flow, flow regimes for horizontal and vertical pipes were examined. The Weisman model and the Mandhane flow regime map were both used. A patented method by which the gas void fraction, GVF is estimated, was examined.

Two Coriolis flowmeters, of two different manufacturers, were tested on an Aerated flow test rig provided by Siemens A/S, Flow Instruments (Nordborg, Denmark). During the tests the back-pressure, the air and liquid fluid parameters were specified and the mass flow rate, density and drive level were measured with the Coriolis flowmeter. The measurement error for the fluid mass flow rate and the fluid density increased as the GVF increased. Meter 2 could measure the drive level which increased as both the GVF and the liquid mass flow rate were increased.

A CFD simulation was designed in order to see the aerated fluid behaviour in the sensor to the Coriolis flowmeter. The CFD simulation was performed using ANSYS workbench and FLUENT. The mixture model and the k-ω turbulence model were used. Based on the FC400 Coriolis flowmeter the mesh for the flow behaviour simulations was made. A grid convergence study was performed using the Grid Convergence Index, GCI, which is based on Richardson Extrapolation.

Three cases were investigated; a steady single-phase case, a transient single-phase case and a transient two-phase case. Recirculation zones in the flowsplitters were first noticed when running the single-phase cases. Three transient two-phase simulations were performed. The inlet parameters changed between a liquid flow rate of 350 kg/h and 3500 kg/h and a GVF of 5% and 10%.

There are areas of a higher gas volume fraction present in all the simulations, than are present in the inlet boundary conditions. These areas increased as either the liquid flow rate increased or the GVF increased, which fits well with the theory of decoupling and the quantified errors of measurements.

An assessment of the validity of the simulation results without oscillations were made with a crude estimation of the forces impact on the flow. The Coriolis force was at least eight times larger that any other force affecting the fluid. It was concluded that the error seen in the experiment, when increasing the GVF, was not caused by the larger Coriolis force but by the decoupling effect. There was no significant change to the size of the Coriolis force when the fluid was pure water or a mixture with a GVF of 5%.

This report contains the first step in improving the measurement accuracy of the Coriolis flowmeter with aerated flow. Several recommendations regarding experiments and simulations are given, these should be seen as the next step in improving the measurement accuracy of the FC430 Coriolis flowmeter.

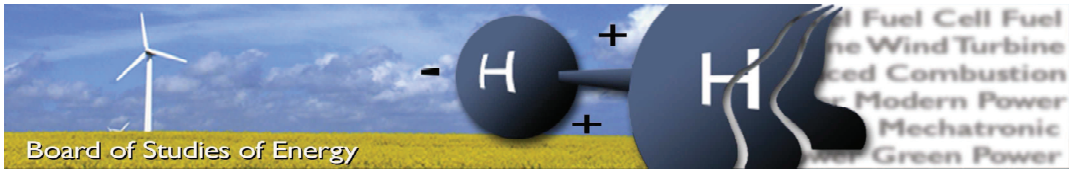

Title:	Aerated flow measurement and modelling of a Coriolis flowmeter
Semester:	4th M.Sc.
Semester theme:	Master's Thesis
Project period:	01.02.14 to 03.06.14
ECTS:	30
Supervisors:	Lasse Aistrup Rosendahl and Thomas Condra
Project group:	TEPE4-1006

Katrine Arnoldsen Juhl

SYNOPSIS:

The purpose of this project is to investigate aerated flow behaviour in Coriolis flowmeters by means of testing two Coriolis flowmeters from different companies and perform Computational Fluid Dynamic, CFD simulations of a SITRANS FC400 sensor to a Coriolis flowmeter under different inlet conditions. The experiments are carried out on an Aerated flow test rig provided by Siemens A/S, Flow Instrument (Nordborg, Denmark). The NAMUR 132 recommendations for the size of the measurement error below a Gas Void Fraction, GVF of 5% is fulfilled. The measurement error and the drive level increases as the GVF increases. The mesh used in the CFD simulations are designed with the knowledge of the two-phase theory and the ERCOFTAC's "Best practices guidelines". The simulations show that there are areas in the flowmeter where the gas volume fraction exceeds the inlet GVF. The areas increases as the inlet GVF increases or the liquid flow rate increase. The simulation results and the theory of decoupling fits well with the experimental results. Several recommendations for improvement of the Coriolis flowmeters performance in aerated flow are listed.

Copies:	4
Pages, total:	96
Appendices:	9
Supplements:	CD

By signing this document, each member of the group confirms that all group members have participated in the project work, and thereby all members are collectively liable for the contents of the report. Furthermore, all group members confirm that the report does not include plagiarism.

Nomenclature

Symbol	Description	Unit
A	Area	m^2
C	Constant	-
c	Speed of Sound	m/s
D	Diameter (inner)	m
d	Diameter (inner)	m
E	Youngs modulus	N/m^2
e_a	Approximately relative errors	-
F	Force	N
F_s	Factor of safety	-
f	Frequency	Hz
g	Acceleration due to gravity	m/s^2
h	Cell number	-
I	Area moment of Inertia	m^4
i	Variable, Indices	-
j	Indices	-
K	Bulk modulus	Pa
k	Turbulent kinetic energy, indices	$J/kg=m^2/s^2$,-
L	Length	m
M	Molecular weight	kg/kmol
m	Mass, mass per unit length	kg, kg/m
n	Constant, number	-
P	Pressure, Residual	Pa,-
p	Order	-
Q	Volume	m^3
q	Variable	-
R	Ideal gas constant, Radius of curvature	J/K·kmol, m
r	Grid refinement ratio	-
S	Slip	-
s	Variable	-
T	Temperature	K

Continued on next page

Continued from previous page

Symbol	Description	
t	Time	s
U	Velocity	m/s
V	Velocity	m/s
x	Distance	m
y^+	Dimensionless wall distance	-
y	Distance between wall and first node away from wall	m
α	Fraction	-
β	Bending constant	-
Δ	Change indicator	-
δ	Boundary layer height	m
ϵ	Fraction	-
ϕ	Solution, angle	Pa,°
γ	Expansion factor	-
κ	Compressibility	1/Pa
λ	No-slip fraction	-
μ	Dynamic viscosity	Pa·s=kg/(s·m)
ν	Kinematic viscosity	m^2/s
θ	Angle	°
ρ	Density	kg/m^3
σ	Surface tension	N/m
ω	Angular velocity, Specific turbulence dissipation rate	rad/s, 1/s

Subscript	
c	Coriolis
d	Dispersed
g	Gas
l	Liquid
gs	Superficial, gas
ls	Superficial, liquid
P	Pressure
R	Resulting
T	Total
x	x-direction
y	y-direction
1	Inlet of bend, mesh number
2	Outlet of bend, mesh number
3	Mesh number

Continued on next page

Continued from previous page

Symbol	Description
Superscript	
$\dot{}$	Rate
c	Continuity
$\vec{}$	Vector

Abbreviations

A-AW	Annular (wavy)
CFD	Computational Fluid Dynamics
D	Dean number
DB	Dispersed bubble
DN	Normal diameter
EB	Elongated bubbles
Eo	Eötvös number
FC	Coriolis Flowmeter
FM	Flowmeter
Fr	Froude number
GCI	Grid Convergence Index
GVF	Gas Void Fraction
GVFA	Gas Volume Fraction Area
HK	Envelopee
I	Slug
Ku	Kutateladze number
LHS	Left Hand Side
Max	Maximum
Min	Minimum
mix	Mixture
Nom.	Nominal
Re	Reynolds number
RHS	Right Hand Side
sccm	Standard Cubic Centimeter per Minute at 0°C and 1 atm.
SD	Standard Deviation
sim	Simulation
SS	Stratified smooth
SST	Shear-Stress Transport
SW	Stratified wavy

Preface

This master thesis has been written for the M.Sc. education Thermal Energy and Process Engineering at the School of Engineering of Science at Aalborg University.

The purpose of this project is to measure and model aerated flow in a Coriolis flowmeter. The performance of the Coriolis flowmeter will be tested on an Aerated flow test rig provided by Siemens A/S, Flow Instrument (Nordborg, Denmark). Simulations of aerated flow in the flowmeter will be performed in order to locate a source of error and achieve an understanding of the theories applied for Coriolis Flowmeters and two-phase flow modelling.

The following programs have been used: MATLAB, Excel, ANSYS Workbench and FLUENT. Some knowledge of these programs are assumed in order to gain full benefit from this report.

Publication of parts of this report is allowed only with references and with written agreement from the author.

Acknowledgment

I would like to thank the R&D department at Siemens A/S, Flow Instruments (Nordborg, Denmark) for their help and information during this project. A special thanks to Nils T. Basse and Thomas Bierweiler for their patience and guidance.

Reading Guide

Throughout the report there will be references to sources used, the sources are placed in the Bibliography. The used method for referring to sources is the Harvard Method, where the source will be written as [Author, Year]. If the reference is included in a sentence before the dot, the reference covers the sentence. If the reference is after a dot, it covers the section or paragragh. If there are more than one source with the same name and year, the source gets a letter after the year. A reference leads to the bibliography where the sources is given by the author, year, title, edition, publisher, hyperlink etc., depending on the source.

Figures, tables and equations are numbered so that it indicates to which chapter they

belong. Appendixes are indicated with a letter. This means that the first figure in Chapter 3 is numbered 3.1 and the next figure is numbered 3.2. The explanatory text will be attached to the given figure or table in a caption.

A CD is attached to the report, which contains data sheets, program files, simulation videos, the report in PDF, PDF copies of all web-sources and articles. The CD appendix refers to the CD sources.

> The sensor geometry, FLUENT cas- and dat-files, the data files from the experiment, the MATLAB and Excel files which handles the data are all confidential, therefore regretfully none of these are included in the report or on the CD.

Cover image from https://www.youtube.com/watch?v=G6L9gKu6lc4

Table of Contents

Chapter 1

Introduction to Coriolis Flowmeter

The principle of measuring amounts of fluids has existed for many hundreds of years; from measuring the number of buckets needed to fill a basin, to now where accurate flowmeters are connected to pipe systems in household and companies all around the world. Flowmeters are a measurement tool which measures the amount and/or the flow rate of fluids. The precise measurements give quality, save money and for a manufacturer it gives a competitive advantage. The quality achieved through the use of a flowmeter is needed in many processes. A couple of examples where a flowmeter is required for precise measuring:

- A flowmeter measures the amount of district heating a house owner uses, so the owners only pay for what they use
- Precise measurement is needed, when measuring large flow amounts of natural gas where a 1% error could represent a very large sum.
- A flowmeter measures the amount of reactants needed in a chemical process which needs to be correct in order to get the right product. A wrong amount of one reactant could make a completely different product with the wrong qualities, which waste money, time, energy, customers and may indeed be life threatening.

There are many types of flowmeters. Electromagnetic, Ultrasonic and Vortex flowmeters measure the volume, whereas Coriolis flowmeters measure the mass flow rate and density. There are several companies on the market which produces Coriolis flowmeters. Some of the companies are Siemens A/S, GE Co., Emerson Electric Co, Endress+Hauser, KROHNE and Micro Motion.

This project is made in cooperation with Siemens A/S, Flow Instruments (Nordborg, Denmark) and will focus on their Coriolis flowmeter series named FC. Siemens have a series of flow measurement devices named SITRANS.

The Coriolis flowmeter made by Siemens works with clean fluids (single-phase fluids) and measures mass flow and density. A Siemens Coriolis flowmeter can be seen in Figure 1.1. The Coriolis flowmeter FC430 have a sensor named FC400 and a transmitter named FC030.

Figure 1.1: Siemens's SITRANS FC430 flowmeter with the sensor FC400 and the transmitter FC030 [Siemens A/S, Flow Instruments, 2014]

Coriolis flowmeters can be mounted on vertical, horizontal or inclined pipelines. They have an attractive accuracy and repeatability; for the FC430 it is ±0.1% and ±0.05%, respectively. [Siemens A/S, Flow Instruments 01 News, 2012] The **accuracy** is the error between the measured density and mass flow, and the actual mass flow and density. The **repeatability** is the error the device can give under the same conditions during the same kinds of test. The accuracy and repeatability is tested in production before dispatch.

The sensor to the Coriolis flowmeter SITRANS FC430 without the casing, can be seen in Figure 1.2. Note that the second tube is hidden under the tube shown. See drawing in Figure I.1 in Appendix I for a more detailed look at the geometry of the flowmeter. On Figure 1.2 (1) indicate Pickup 1, (2) indicate the driver and (3) indicates Pickup 2.

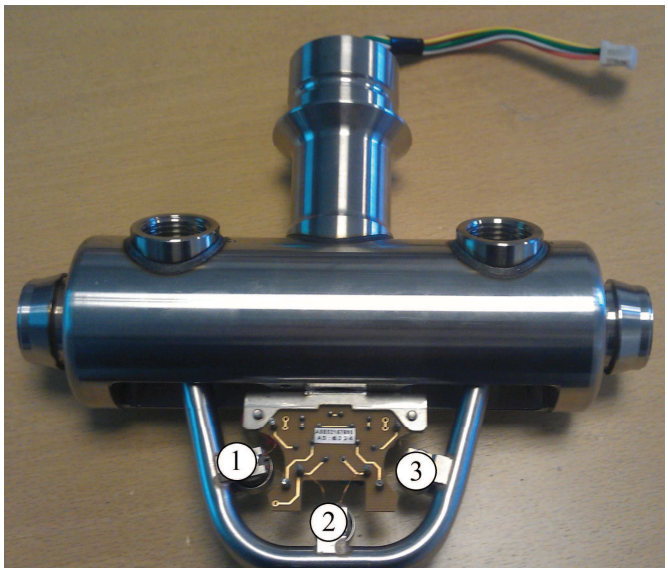

Figure 1.2: The Siemens SITRANS FC400 sensor DN15. (1) indicate Pickup 1, (2) the driver and (3) Pickup 2

"The SITRANS FC sensors are energized by an electromagnetic driver circuit which oscillates the pipes at their resonance frequency. Two pickups are placed symmetrically on either side of the driver to provide position signals for digital processing." [Siemens A/S, Flow Instruments, 2012]
When a fluid flows through the flowmeter, Coriolis force will act on the measuring tubes and cause a deflection which can be measured as a phase shift between Pickup 1 and Pickup 2, see Figure 1.3.

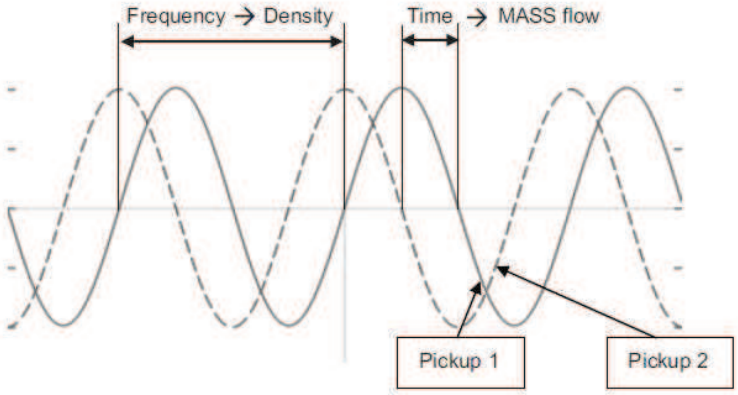

Figure 1.3: The pickup signals [Siemens A/S, Flow Instruments, 2012]

The Coriolis effect is a force experienced by a moving object when it is viewed in a rotating frame. Figure 1.4 shows the Coriolis force created by the moving fluid in the Coriolis flowmeter. A clockwise rotation of the reference frame, $\vec{\omega}$ gives a deflection, created by the Coriolis force, $\vec{F_c}$, which is to the left of the motion, $\vec{V}$ of the object, m. A counter clockwise rotation gives a deflection to the right. In the flowmeter the vibration set in motion by the driver coil gives the rotating reference frame and the fluid is the moving object. [Weinstein, 2008]

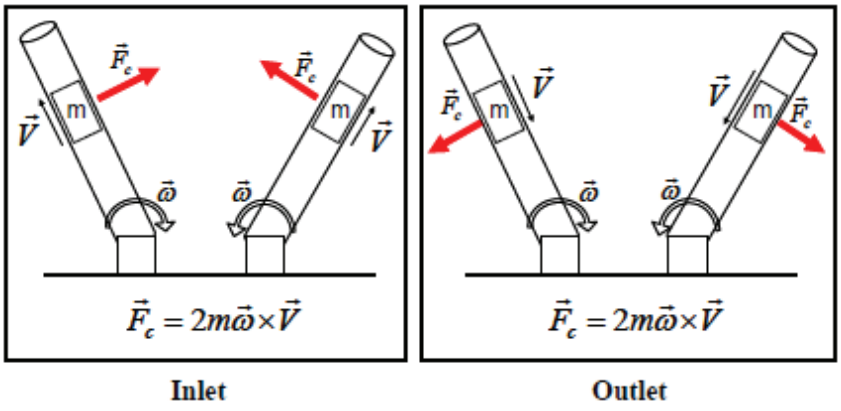

Figure 1.4: Coriolis force on the inlet and outlet flow tubes [Weinstein, 2008]

If a fluid passes through the tubes, the tubes have a wriggling motion, which gives a phase shift between inlet and outlet pickups. The pickup sensors measures the spatial displacement in time. The phase shift gives the mass flow and the frequency gives the

density. At zero flow conditions the pickup sensors are synchronized to each other. The tubes in the flowmeter vibrate at their resonance frequency, but when the fluid density changes, the tube frequency changes as well. The denser the medium through the Coriolis flowmeter the lower the resonance frequency *i.e.* a water filled tube will oscillate at a lower frequency than that of a tube filled with air.

The resonance frequency dependency of the fluid mass can be illustrated by looking at a simple beam fixed in both ends. Equation (1.1) shows the frequency of a beam fixed in both ends with Young's modulus E, area moment of inertia I, length of beam L and mass per unit length m. When the mass per unit length increase the frequency decreases. [University of Massachusetts Lowell, 2014]

$$f = \frac{1}{2\pi}\beta\sqrt{\frac{EI}{mL^4}} \tag{1.1}$$

β is a constant which depends on the order n of bending *i.e.* first-order, second-order and so forth.

The phase shift is linearly dependent on the mass flow rate for a single-phase fluid. Whereas the frequency is linearly dependent on the density for a single-phase fluid. [Daniel L. Gysling, 2007]

1.1 Two-Phase Fluid in Coriolis Flowmeter

The attractive accuracy and repeatability for Coriolis flowmeters are only valid for single-phase fluids. Two-phase fluid flow in the the Coriolis flowmeter gives unacceptable measurement errors. Two-phase fluid flow can be a combination of solids, liquids and gases. In this project a two-phase flow refers to an aerated flow. The continuous phase is water and the dispersed phase is air. The Gas Void Fraction, GVF will be between 0 and 10%. 10% GVF corresponds to an air mass fraction of approximately 0.001, which can be seen in Figure 1.5. The definition of the GVF can be seen in Equation (C.12) in Appendix C.

Figure 1.5 shows how the dimensionless air mass flow rate and the GVF are not related linearly. Figure 1.5 is based on Equation (C.12) in Appendix C, where the liquid mass flow rate, gas and liquid densities are constants and only the gas mass flow rate, and thereby the GVF, varies.

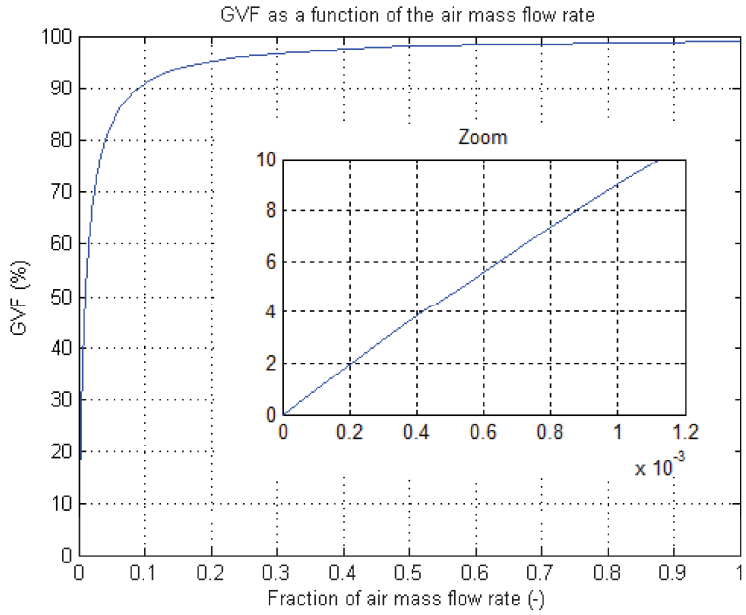

Figure 1.5: GVF as a function of air mass flow rate fraction

1.1.1 Compressibility Error

Aerated liquids are significantly more compressible than non-aerated liquids. This is due to the compressibility of a fluid is related to the density and speed of sound of the liquid. Figure 1.6a shows the speed of sound of a mixture dependent on the GVF. Figure 1.6a is based on Equation (C.13) in Appendix C. The left side of the graph represents the speed of sound for pure liquid whereas the value on the right is the speed of sound for pure gas. The flow regime is dispersed, see Chapter 2 for further information on flow regimes.

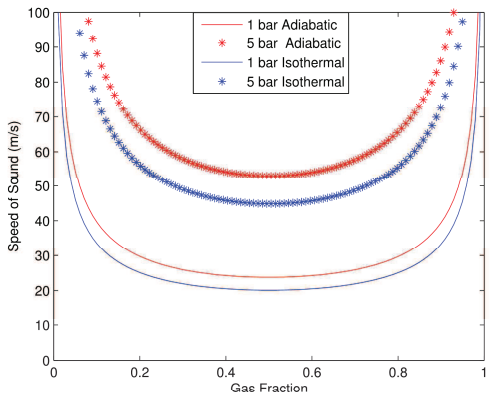

(a) The speed of sound dependency on GVF

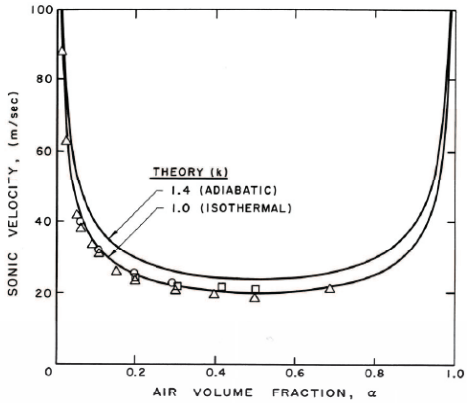

(b) Speed of sound for a bubbly air/water mixture at atmospheric pressure. Experimental data from Karplus (1958) and Gouse and Brown (1964) [Brennen, 2005]

Figure 1.6: Speed of sound in a mixture of air and water. Note that the y-axis is chopped

Figure 1.6a is based on the dispersed flow regime at 1 and 5 bar. Here the maximum speed of sound for liquid is 1475 m/s and 343 m/s for gas (adiabatic). The dispersed flow regime has a lower speed of sound when the pressure decreases. At 1 bar, adiabatic with 50% air in the mixture the speed of sound is approximately 24 m/s at 15°C.

Figure 1.6b show that the equation for speed of sound (Equation (C.13) in Appendix C) in a mixture is consistent with earlier experiments and literature.

The compressibility of a mixture can be found with Equation (1.2) where ϵ_i is the volumetric phase fraction of component i and c_i is the corresponding speed of sound. [Daniel L. Gysling, 2007]

$$\kappa_{mix} = \sum_{i=1}^{n} \frac{\epsilon_i}{\rho_i c_i^2} \tag{1.2}$$

Air at 20°C atmospheric pressure is approximately 15000 times more compressible than water. Thus adding 1% air to the water increases the compressibility of the mixture by a factor of approximately 150.

1.1.2 Decoupling Error

The same volume of gas bubbles and liquid will accelerate differently due to their difference in mass. Gas bubbles experience higher acceleration than the fluid surrounding it, which leads to relative motion between the bubbles and the fluid. This causes mass and density measurement errors due to the change in the location of the centre of gravity of the fluid mixture inside the tube. This error is called the decoupling error. [Weinstein, 2008]

For a single phase case there is only one type of fluid inside the tube. The centre of gravity and the centre of the fluid move together; and there is no error associated with decoupling. Figure 1.7 is a simple sketch of the fluid behaviour in the pipe. The green diamond is the centre of gravity, which lies in the centre of the pipe.

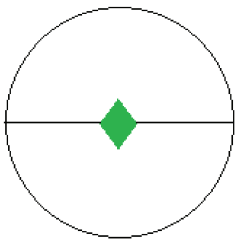

Figure 1.7: Single-phase fluid behaviour

For two-phase flow the centre of gravity and the centre of the fluid move separately from each other due to, for example, an aerated liquid. In the simple sketch in Figure 1.8 the centre of gravity (green diamond) and the bubble (blue circle) move when the flowmeter vibrates vertically.

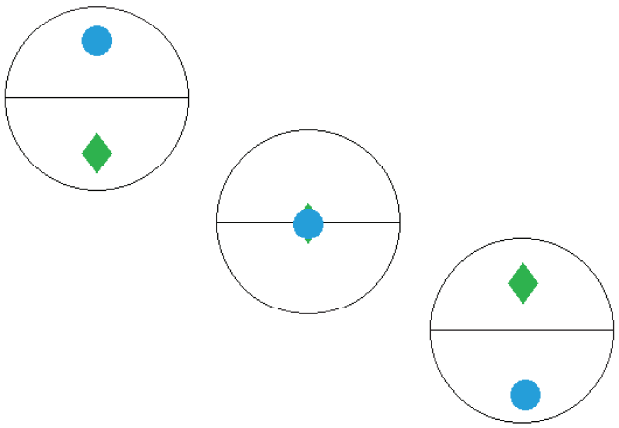

Figure 1.8: Two-phase fluid behaviour with vertical vibrations

The size of the error depends on the dynamic viscosity of the gas. At high liquid viscosity there is little motion of the actual bubble and therefore very little motion of the centre of gravity, which gives small decoupling errors. For low viscosity the bubbles can move further on each oscillation, than in the high viscosity case, which generates larger errors.

Damping due to Decoupling

The drive coil has an amount of drive power available to create the oscillations in the tubes, which is called the **drive power**. In single phase flow the drive power used and the tube amplitude are steady at nominal values. The tube amplitude range is a few micrometers. The drive power increases rapidly as the GVF increases. As the maximum of the drive power is being reach, the tube amplitude begins to fall. If the GVF continues to rise, the maximum of the drive power is reached and the amplitude reaches the minimum value, where the tube is only driven by flow turbulence (noise). The measurement error in the mass flow rate and density increases as the GVF increases. At GVF higher than 10% the flowmeter has unacceptable errors and at higher GVF it will fail to function properly. [Basse, 2014b]

1.2 Thesis Statement

Coriolis flowmeters measure the mass flow rate of a fluid, the density and temperature and have an accuracy of 0.1% in single-phase flows. Aerated flow in the Coriolis flowmeter causes some unacceptable measurement errors due to decoupling and compressibility created by air bubbles. The mass flow rate can be found using the phase shift and the density by the frequency. The flow regime in the flowmeter depends on the Gas Void Fraction, GVF.

By knowing the effect the flow regimes have on the flowmeter and its measurements, it is possible to develop a method which compensates and uses the raw mass flow rate and density readings in order to generate corrected data.

This report will account for two-phase fluid flow regimes, GVF estimation and how different GVF will effect various Coriolis flowmeters. The effect of the GVF will be investigated using Computational Fluid Dynamics, CFD on a SITRANS FC400 DN15 sensor geometry. The designed mesh, solution method and results will be presented. Finally, a summary of the GVF effect on the performance of the Coriolis flowmeter will be given.

The flowchart in Figure 1.9 shows the process chain for product improvements. Quantify the measurement errors and simulate the flow behaviour in the Coriolis flowmeter without oscillations, are the scope of this report and is seen as the first step towards improving the measurement accuracy for aerated flows in Coriolis flowmeters.

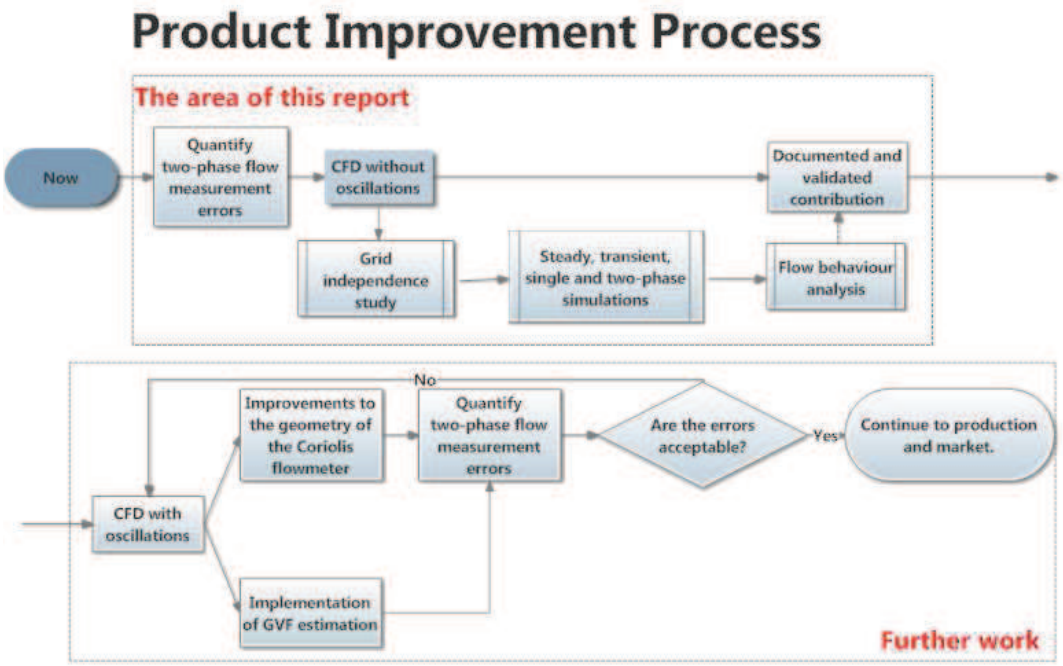

Figure 1.9: Process chain for product improvement

To make improvements to the Coriolis flowmeter there are several steps after this report before the Coriolis flowmeter can go into production and to the market.

Goals

The project can be divided into several goals which has to be fulfilled in order to obtain a solid and well evaluated project.

- Show the Coriolis flowmeter and its purpose.
- Explain two-phase flow impact on Coriolis flowmeter
- Explain the flow regimes in two-phase flow
- Test different Coriolis flowmeters with aerated flow.
- Quantify the measurement errors
- Set up a CFD model which can be run transient and steady with single-phase and two-phase flow
- Investigate steady single-phase grid independence to find an acceptable mesh for the Coriolis flowmeter using the Grid Independence Index
- Perform a transient simulation which predict the bubble behaviour in the flowmeter
- Summarize the two-phase flow impact on the Coriolis flowmeter
- Assess the simulation results and estimate the impact from oscillations on the flow
- Evaluate and determine the next step in the product improvement process

Limitations and Assumptions

The limitation and assumptions for the project.

- CFD modelling is performed without taking the vibrations into account
- Assuming dispersed bubble flow at the entrance to the Coriolis flowmeter
- Slip is assumed in the simulation. The flow is not considered to be homogeneous

Chapter 2

Flow Regimes in Two-Phase Flow

In single-phase flow, the type of the flow can be characterised as laminar or turbulent. Two-phase flow is further characterised by flow regimes, that are characteristic for the space and time distribution of gas and liquid flow. In Appendix C the fluid definitions and properties for two-phase flow are defined and described. The flow regime depends on the orientation of the pipe and are generally divided into horizontal and vertical flows.

2.1 Horizontal Flow

In horizontal flow the flow regimes are divided into stratified, slug, dispersed bubble and annular flow. The flow regimes can be seen in Figure 2.1.

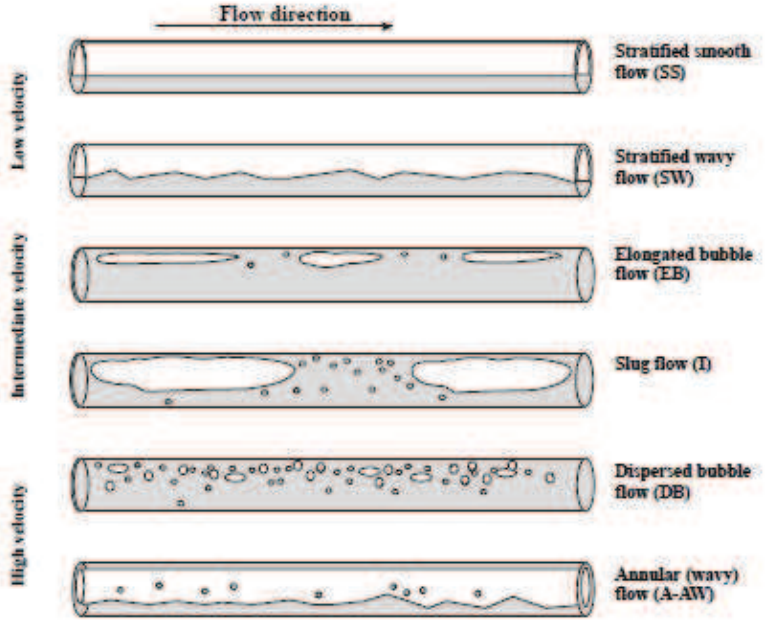

Figure 2.1: Horizontal flow regimes in two-phase flow [Time, 2009]

The gas and liquid at low velocities separates into a stratified flow. As the velocities increase the gas and liquid mixes and the regime goes from slug flow to dispersed bubble flow. At high velocities the liquid can be carried as bubbles in the gas, which is known as the annular regime.

The Weisman model is a set of correlations based on experiments in pipes with different diameters used with various fluids. It assumes horizontal pipe orientation and a gas-liquid flow. The input parameters are the pipe diameter, liquid and gas density, viscosity and superficial velocities and the surface tension between the two phases. The Weisman model is based on four equations [Time, 2009]. The equations include several dimensionless quantities; Reynolds Re, Froude Fr, Kutateladze Ku and Eötvös Eo. Appendix B elaborates on the dimensionless numbers. The constants and variables can be found in the nomenclature list.

Stratified-intermittent transition (if LHS < RHS then intermittent)

$$\begin{aligned} 0.25\left(\frac{U_{gs}}{U_{ls}}\right)^{1.1} &= \frac{U_{gs}}{\sqrt{gD}} \\ &= (Fr_g)^{1/2} \end{aligned} \tag{2.1}$$

Intermittent covers elongated bubbles and slug flow. LHS means Left Hand Side and RHS is Right Hand Side.

Transition to annular flow (if RHS>LHS then annular)

$$\begin{aligned} 1.9\left(\frac{U_{gs}}{U_{ls}}\right)^{1/8} &= \left\{\frac{U_{gs}\rho_g^{1/2}}{\left[g\left(\rho_l-\rho_g\right)\sigma\right]^{1/4}}\right\}^{0.2}\left(\frac{U_{gs}^2}{gD}\right)^{1.8} \\ &= Ku^{0.2}Fr_g^{1.8} \end{aligned} \tag{2.2}$$

Transition to dispersed flow (if LHS<RHS then dispersed)

$$\begin{aligned} 1.7 &= \left(\frac{\left(\frac{dP}{dx}\right)_{ls}}{\left(\rho_l-\rho_g\right)g}\right)^{1/2}\left(\frac{\sigma}{\left(\rho_l-\rho_g\right)gD^2}\right)^{-1/4} \\ &= \left(\frac{\left(\frac{dP}{dx}\right)_{ls}}{\left(\rho_l-\rho_g\right)g}\right)^{1/2}\left(\frac{1}{Eo}\right)^{-1/4} \end{aligned} \tag{2.3}$$

$$\begin{aligned} \left(\frac{dP}{dx}\right)_{ls} &= \frac{4}{D}\cdot C_l\cdot\left(\frac{U_{ls}D}{\nu_l}\right)^{-n}\cdot\frac{1}{2}\rho_l U_{ls}^2 \\ &= \frac{4}{D}\cdot C_l\cdot\left(Re_{ls}\right)^{-n}\cdot\frac{1}{2}\rho_l U_{ls}^2 \end{aligned} \tag{2.4}$$

Where the constants C_l and n depend on the liquid superficial Reynolds number which is defined below. The liquid superficial Reynolds number uses the liquid superficial velocity, the liquid density and liquid viscosity. These are all defined in Appendix C.

$$Re_{ls} = \frac{U_{ls}D\rho_l}{\mu_l}$$

If Re_{ls}>4000

$$C_l = 0.046 \qquad n = 0.02$$

If the liquid superficial Reynolds number is lower than 4000, then the constants will be

$$C_l = 16 \qquad n = 1$$

Transition between stratified flow with and without waves (if LHS<RHS then stratified wavy)

$$8\left(\frac{U_{gs}}{U_{ls}}\right)^{0.16} = \left(\frac{\sigma}{(\rho_l - \rho_g)\, gD^2}\right)^{0.2} \left(\frac{U_{gs}\rho_g D}{\mu_g}\right)^{0.45} = \left(\frac{1}{Eo}\right)^{0.2} (Re_{gs})^{0.45} \tag{2.5}$$

The Weisman model can predict the flow regimes but only for horizontal flows. Figure 2.2 shows a flow pattern map proposed by [Mandhane et al., 1974], commonly known as the Mandhane flow regime map. It is a simple two-dimensional map which is based on 1178 observations for a air-water horizontal pipe system and tested on 5935 individual flow pattern observations. The Mandhane flow regime map is an "average" of three other flow pattern maps; Baker (1954), Hoogendoorn (1959) and the revised Govier and Omer (1972). The parameters used in this project fits within the range of parameter values for data used in designing the flow pattern map. The coordinate axes are the superficial velocities for the gas and liquid respectively. The red circles represents a fluid with a liquid flow rate of 350 kg/h and 3500 kg/h which is added a 5% GVF in a straight pipe with the inlet diameter of the flowmeter.

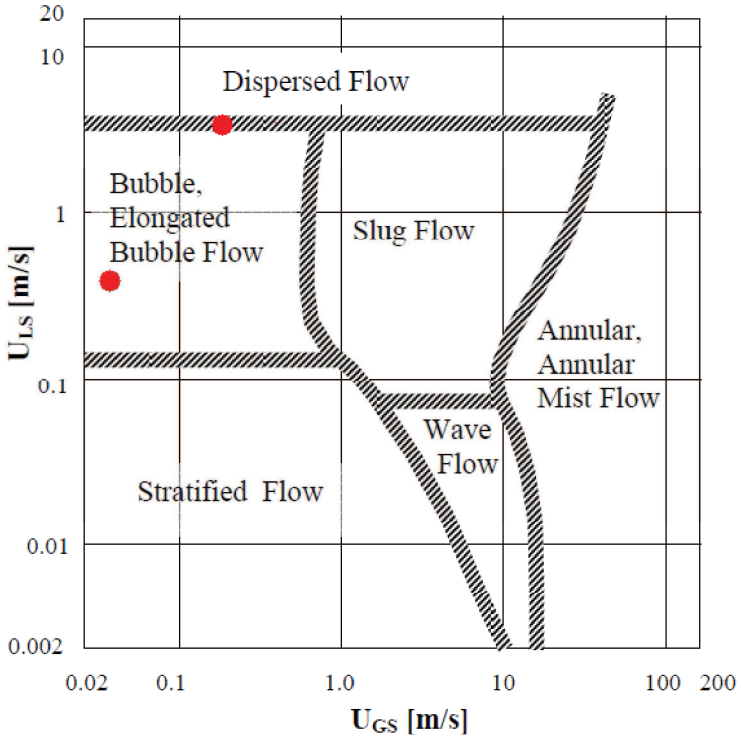

Figure 2.2: Mandhane flow regime map in SI units by [Time, 2009]

The transition boundaries in the flow map should be viewed as transition regions since the map represents an average compromise over a wide variety of combinations of physical properties and pipe diameters. [Mandhane et al., 1974]

2.2 Vertical Flow

The vertical flow does not have the stratified regime. Instead there is the slug, churn, dispersed bubble and annular flow as seen in Figure 2.3. Slug flow has low velocity Taylor bubbles. Taylor bubbles are slug bubbles which are shaped as a bullet.

As the velocities increase the Taylor bubbles break up and the flow regime goes to churn and then later to dispersed bubble flow. At high velocities in the annular flow regime the liquid lies as a film on the circumference of the pipe and the gas transport liquid droplets up through the pipe.

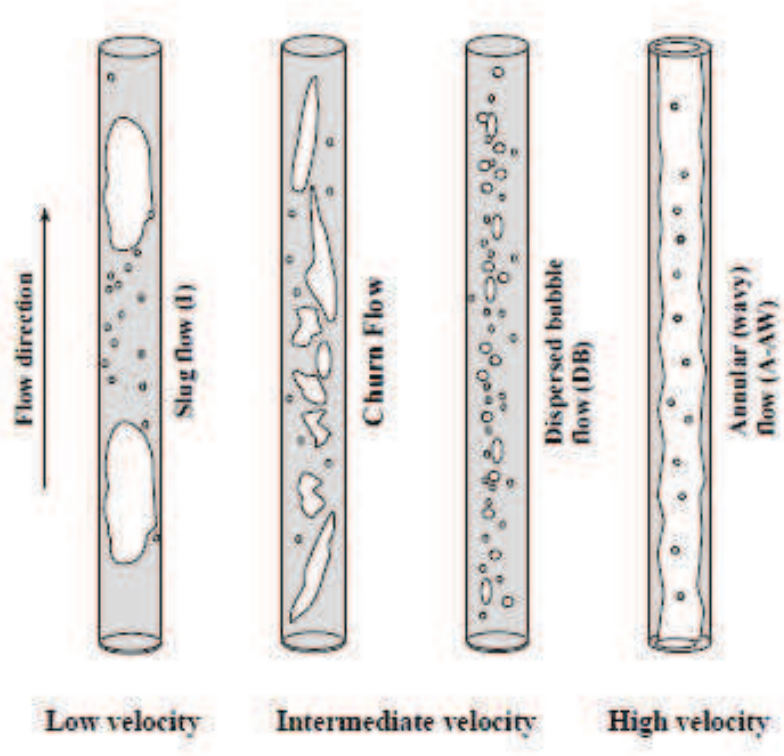

Figure 2.3: Vertical flow regimes in two-phase flow [Time, 2009]

In the Coriolis flowmeter horizontal and angled flow are presented. Experiments have shown that the Coriolis flowmeter do not handle the slug flow as well as the dispersed bubble flow due to the tubes curvature [Basse, 2014b]. The flow regime cannot be observed when the flowmeter is used but must be determined in order to have a properly working flowmeter.

2.3 Evolution of the Estimation Procedure for GVF

Due to the damping from the aerated flow the estimation of the GVF is not so simple. The patent EP2297552B1 [Bierweiler et al., 2010] describes how to estimate the GVF in aerated flow. The concept of GVF estimation is here explained based on [Bierweiler et al., 2010] and [Bierweiler, 2014]

From the pickups the frequency and the phase shift are measured. The standard deviation of the frequency, SD(f) and the phase shift, SD(ϕ) are calculated. By the use of Inverse Envelopes[1], HK^{-1} the minimum and maximum GVF based on the standard deviation of the frequency and the phase shift can be estimated, see Equations (2.6) and (2.7).

$$GVF_{minSD(f)} = HK^{-1}(SD(f)) \qquad GVF_{minSD(\phi)} = HK^{-1}(SD(\phi)) \tag{2.6}$$

$$GVF_{maxSD(f)} = HK^{-1}(SD(f)) \qquad GVF_{maxSD(\phi)} = HK^{-1}(SD(\phi)) \tag{2.7}$$

The Inverse Envelopes are created based on two parametric fields, which are obtained for each sensor size for different flow rates, back pressures and GVFs. The parametric fields are made from experiments where the amplitude and driver level are functions of the GVF. The piece-wise linear enveloping functions are divided into a minimum and maximum envelope based on the parametric field.

Figure 2.4 shows the graphs from the patent.

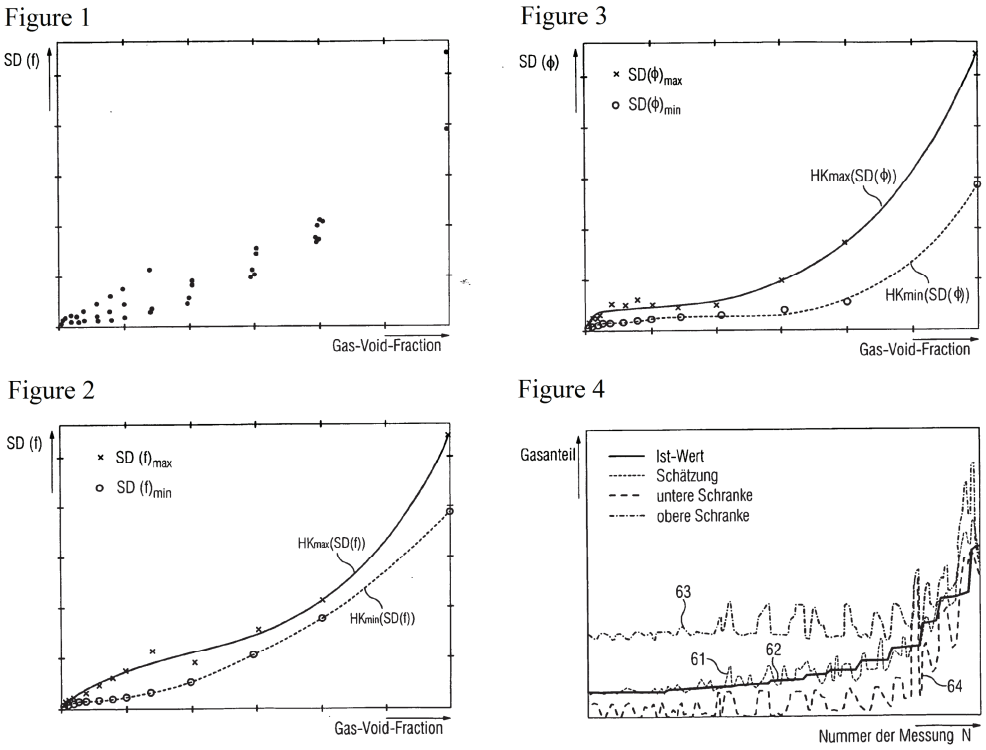

Figure 2.4: Pictures from the patent [Bierweiler et al., 2010]

[1]The concept of Inverse Envelopes is an invention of the inventors.

Figure 1 shows the experimental results. Figure 2 and 3 show the envelopes. Figure 4 shows the GVF estimate. The numbers in Figure 4 corresponds to four GVF functions. 61 is the GVF estimate. 62 is the actual GVF. 63 is the upper bound $\mathrm{GVF}_{\max}$ and 64 is the lower bound $\mathrm{GVF}_{\min}$.

In order to improve the GVF estimation, several envelope functions (sets) can be developed and used. The flowmeter will then have to switch between the envelope sets depending on either the drive power, mass flow rate or some other parameter.

By comparing the minimum and maximum ranges of the GVF estimation from Equation (2.6) and (2.7), the true maximum and minimum range can be found, see Equation (2.8).

$$\begin{aligned} \mathrm{GVF}_{\min} &= \max(\mathrm{GVF}_{\mathrm{minSD}(f)}, \mathrm{GVF}_{\mathrm{minSD}(\phi)}) \\ \mathrm{GVF}_{\max} &= \min(\mathrm{GVF}_{\mathrm{maxSD}(f)}, \mathrm{GVF}_{\mathrm{maxSD}(\phi)}) \end{aligned} \tag{2.8}$$

These are average and the estimated GVF is found in (2.9).

$$\mathrm{GVF}_{\mathrm{estimated}} = \left(\mathrm{GVF}_{\min} + \mathrm{GVF}_{\max}\right)/2 \tag{2.9}$$

This technology is not yet implemented in the Coriolis flowmeter. Siemens A/S, Flow Instruments have focused on other improvements of their Coriolis Flowmeter but wishes to implement a GVF estimation in the Coriolis flowmeter and this project will contribute to this aim.

Chapter 3

Benchmarking of Coriolis Flowmeters

The Coriolis flowmeter is known to handle aerated flow with unacceptable measurement errors. In order to quantify these errors an experiment is set up where two Coriolis flowmeters from two different companies are tested. The flowmeters has been tested on the flow rig provided by Siemens A/S, Flow Instruments. See more information about the test procedure and the test rig in Appendix D and the flowmeters in Appendix I. An air flow controller and a reference Coriolis flowmeter, measuring only the liquid flow rate and density, give expected values of the density and mass flow of the mixture. Three parameters have been changed in the experiment: (1) the mass flow rate of water, (2) the back-pressure and (3) the GVF which were changed in steps. The maximum GVF was 10% in all the experiments. Two flowmeters from two different companies were tested on the flow rig.

Several other flowmeters were scheduled to be tested, but unfortunately the flow rig broke down under another unrelated test and could not be repaired in time to test the other Coriolis flowmeters.

Figure 3.1 is an example of one of the results from the experiment.

Average Mass Flow Error [%]

RIG Preesure setting [mBar rel]	(Mehrere Elemente)
Data Validity	Valid

Average of Mass flow error (diff.) [%]	Nom.Flow: 9%	18%	26%	35%	51%	69%	86%	101%
GVF [%]	325	650	975	1300	1900	2550	3200	3750
0	-0.02	-0.01	0.00	-0.01	0.00	0.00	-0.02	-0.01
0.2	-0.01	0.00	0.00	0.00	0.00	0.00	-0.01	0.01
0.3	0.00	0.00	0.00	0.00	0.00	0.00	0.00	0.01
0.5	0.01	0.00	0.06	0.00	0.00	0.00	-0.03	-0.08
0.7	-0.01	0.00	0.00	0.00	0.01	0.01	0.02	0.03
1	0.00	0.00	-0.01	0.08	0.24	0.23	0.23	0.32
2	0.02	-1.15	-0.31	0.80	2.31	1.86	1.17	0.68
5	1.10	-16.17	-5.69	2.48	6.94	4.48	-0.20	-2.21
10	-12.50	-47.88	-31.25	-9.45	8.80	5.11	-3.19	-9.44

Error code
0.00
0.10
0.25
0.50
1.00
2.00
5.00
10.00
20.00
50.00
100.00

Figure 3.1: Flowmeter 1 test result averaged over all back-pressures with error code

Figure 3.1 shows the results for the averaged mass flow error (%) averaged over all back-pressure. The nominal flow rate for the flowmeters are 3700 kg/h and 3800 kg/h for Meter 1 and Meter 2, respectively. The liquid flow rate used in the experiment varied from 250 kg/h to 3750 kg/h and the GVF varied from 0 to 10%. The table is error coded in order to make the deviation easier to see. The more red a cell is, the higher the error in percentage. The error code explanation is in the right side of Figure 3.1.

Figure 3.1 shows clearly that Flowmeter 1 has accuracy problems when the GVF increases. The mass flow rate and the density are the measured parameters. The mass flow error is found from Equation (3.1). The mass flow referred to is the mixture mass flow.

$$\text{Error}_{\dot{m}} = \left(\frac{\text{Measured mass flow - Expected mass flow}}{\text{Expected mass flow}} \right) \cdot 100 \tag{3.1}$$

Figure 3.2 shows the averaged mass flow error for the different meters and the maximum of the mass flow error. The maximum and averaged errors are found based on the averaged different back-pressures and averaged over the different flow rates. Meter 2 has small errors both positive and negative in the low GVF area below 5%. As the GVF increases above 0.7% Meter 1 experiences some errors as well. Comparing the data from Meter 1 and Meter 2 at the GVF of 5 and 10% show a drastic increase in the averaged mass flow error for Meter 1. The results indicate that at GVF below or equal to 5% Meter 1 measures the mass flow more precisely than Meter 2.

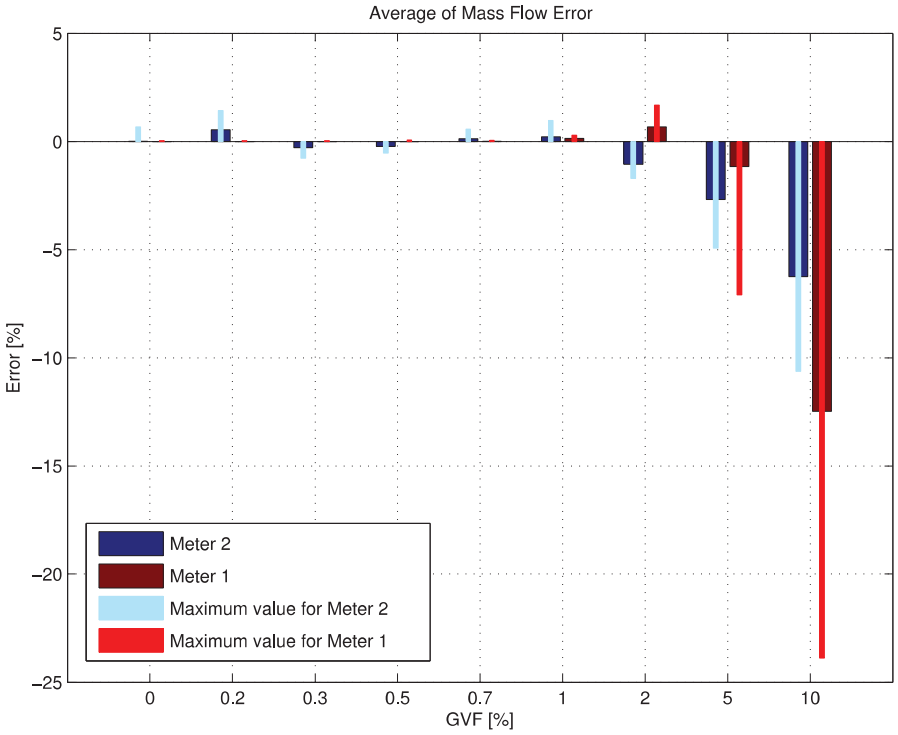

Figure 3.2: Average and maximum mass flow error

The density error is found from Equation (3.2), where the expected density is the mixture density calculated as in Equation (C.9) in Appendix C.

$$\text{Error}_\rho = \left(\frac{\text{Measured density - Expected density}}{\text{Expected density}} \right) \cdot 100 \tag{3.2}$$

Figure 3.3 shows the averaged and maximum density errors for the different meters. The averaged density is measured to be higher than expected, at low GVF, around 0.2% to 2%. At GVF higher or equal to 5% the averaged density error has a high negative error, which means the measured density is lower than the expected density, see Equation (3.2). Comparing the averaged of mass flow error (Figure 3.2) and the average of density flow error (Figure 3.3) show, that Meter 1 measures the mass flow rate more precisely than Meter 2 at GVF below or equal to 5%, but the density measurement accuracy is approximately equal at a GVF below or equal to 1%.

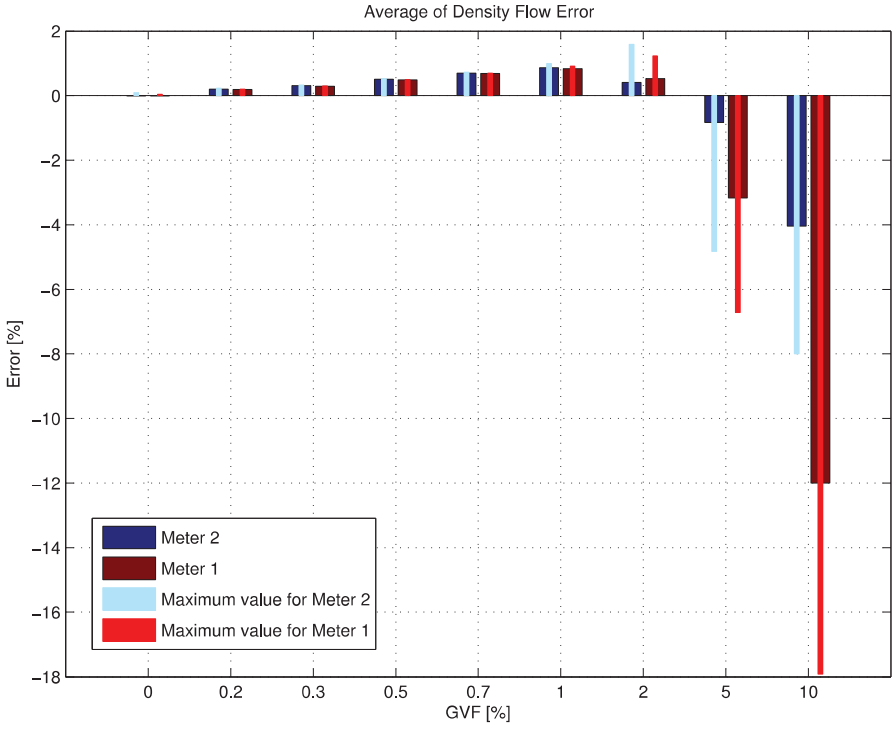

Figure 3.3: Average and maximum density error

The drive level is a percentage of the available drive power. The drive power is the power, which is used to vibrate the tubes. For Meter 2 the drive level, in water flow without air, will be between 0 and 1%. The drive level will increase significantly if air is present or the single-phase fluid has a high viscosity. In the experiment the drive level is increased as the liquid flow rate and the GVF is increased, according to Figure 3.4.

Average of Drive Level

Choose sensor size:	15
RIG Pressure setting [mBar rel]	(All)
Data Validity	Valid

GVF [%]	Nom.Flow: 7% 250	14% 500	20% 750	27% 1000	34% 1250	41% 1500	47% 1750	54% 2000	68% 2500	81% 3000	95% 3500
Mittelwert von Drive level											
0	3.08	3.44	3.19	3.07	3.07	4.09	4.42	3.10	3.16	3.23	3.37
0.2	3.05	3.31	3.15	3.07	3.07	3.79	5.05	3.10	3.15	3.24	3.34
0.3	3.14	3.44	3.08	3.07	3.07	3.43	3.08	3.09	3.14	3.23	3.33
0.5	3.14	3.02	3.24	3.07	3.07	3.08	3.08	3.09	3.15	3.24	3.36
0.7	3.14	3.34	3.10	3.07	3.07	3.07	3.08	3.09	3.15	3.24	4.62
1	3.14	3.16	3.07	3.06	3.07	3.75	4.04	7.29	8.35	8.54	16.16
2	3.14	3.48	3.13	6.16	7.84	16.16	29.55	34.17	56.97	52.69	53.26
5	3.14	3.31	11.12	11.84	29.14	34.42	53.42	69.52	98.39	100.00	100.00
10	3.14	19.94	37.84	41.12	41.95	77.55	81.33	71.94	98.19	100.00	100.00

Figure 3.4: Drive level for Meter 2 averaged over the different back-pressures

It is observed that the GVF has no significant impact on the drive level when the liquid flow rate is low (250 kg/h). As the liquid flow rate increases the size of the GVF has an impact on the measurement error size. At GVF below 1% the liquid flow rate size has no impact on the measurement error size.

Figure 3.5 shows the values in Figure 3.4 as a plot. It is observed that at low GVF (below 0.7%) the drive level is constant, but when the GVF increases the drive level increases rapidly. When the meter power output reaches maximum, the amplitude begins to fall, which is where the significant errors in the density and mass flow readings occurs. In Figure 3.5 the test which runs with a liquid flow rate of 2500, 3000 or 3500 kg/h all reaches the maximum drive level when they have a GVF of 5% or more.

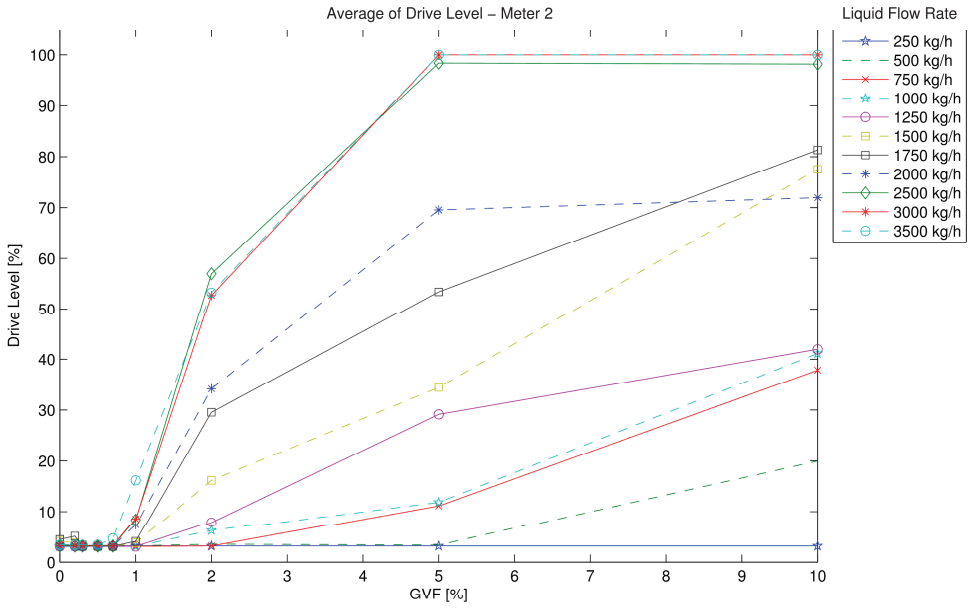

Figure 3.5: Drive level as function of GVF and liquid flow rate

The author hypothesizes that the measurement error experienced is connected to the maximum drive level. So if the maximum of the drive level were increased the errors in density and mass flow readings would decrease. This hypothesis requires further testing and system changes to the Coriolis flowmeter in order to see if a change of maximum drive level would increase the Coriolis flowmeter accuracy in aerated flows.

There seems to exist a critical value which combines the GVF and the liquid flow rate for which the error of the drive level increases after this. The author suggest the dimensionless Dean number to explain the critical value. The Dean number, which is used when studying flows in curved pipes, can be seen in Equation (3.3).

$$D = Re\left(\frac{d}{2R}\right)^{1/2} \tag{3.3}$$

In Equation (3.3) d is the diameter of the Coriolis tube and R is the radius of curvature of the tube. The Reynolds number would in this case be the mixture Reynolds number. The Dean number decreases as the liquid flow rate decreases. The GVF has only a small impact on the mixture Reynolds number as seen later in Section 4.1 in Figure 4.2. The Dean number, at a constant mixture Reynolds number, decreases if the radius of curvature of the tube increases and hereby increasing the measurement accuracy.

3.1 Summary of Tests

Experimental tests have been performed with two Coriolis flowmeters from two different companies. The flowmeters have been tested at varying liquid flow rates, GVF's and back-pressures. The flowmeters are compared on mass flow rate errors and density errors. In addition to these tests it was possible to perform a drive level test for Meter 2.

The accuracy of the SITRANS FC430 is claimed to be ±0.1% for single-phase fluids in Chapter 1. The experiments with the two flowmeters show that this claim is valid when having a fluid with a GVF of 0%.

The NAMUR recommendations are the written ambitions and desired preferences for the flow industry. Paraphrasing the NAMUR recommendation 132 for measuring mass flow with aerated flow with Coriolis flowmeter; "the mass flow measurement error should not be greater than the percentage GVF of up to approx. 5%". [NAMUR Recommendation, 2009]

Meter 1

At GVF below or equal to 2% the averaged mass flow errors are below 1% and at GVF higher than 2% the error increases as the GVF increases. The flowmeter measures at GVF below 5% a higher density than expected and at higher GVF the density is measured several percentage under the real density. After 2% GVF the density error increases as the GVF increases, below 2% the error lies between 0 and 1%.

Meter 1 has large density errors at a GVF between 5% and 10%. The average mass flow and density measurements below 5% GVF meets the NAMUR recommendations.

Meter 2

Meter 2 complies with the NAMUR recommendations 132 since the mass flow measurements are not greater than the GVF in percentage when looking at the averaged mass flow error except at a GVF of 0.2%. The maximum of absolute mass flow error almost fulfils the NAMUR 132 recommendations also. The density error both the maximum and the average at the low GVF; 0.2, 0.3, 0.5 the density error lies just above the NAMUR recommendations. The average mass flow at low GVF has both positive and negative errors, which is below 1% deviation. An explanation for the increase in both density and mass flow rate errors is the increase in the drive level after a GVF of 5%. Figure 3.5 shows that the drive level increases to the maximum level at high GVF and high liquid flow rates.

Chapter 4

CFD

A CFD simulation of the Coriolis flowmeter with two-phase flow would give some insight into the fluid behaviour and might explain why the experiments showed an increase in the size of the measurement error as the GVF and the liquid flow rate increases.

First in this chapter several meshes will be designed which take the wall influence into consideration. In Section 4.2 a grid independece analysis will be performed and a mesh design will be chosen. The simulations will be performed with ANSYS FLUENT 14.0. The FLUENT setup and boundary conditions will be explained. The simulations will be presented in Chapter 5

The CFD simulation will not take the vibration of the tubes into considerations since the perpendicular motion to the fluid is extremely small [Basse, 2014b]. The symmetry of the Coriolis flowmeter is used when defining the solution domain. Only one tube and half of the inlet, outlet and flowsplitters are meshed.

4.1 Mesh Design Parameters

The Coriolis flowmeter domain needs to be meshed in order to run a simulation showing the aerated flow behaviour. The geometry, as seen in I.1 in Appendix I, is complex with its flowsplitters and tubes. The Coriolis flowmeter creates a pressure loss across the flow tubes, which means that the GVF is not constant but increases through the meter. At nominal single-phase flow the pressure loss is approximately 1 bar over the flowmeter. The water flow rate and the pressure decides how large the GVF is.

Figure 4.1 shows the minimum possible GVF in a straight pipe when the air provided is 40 sccm at 0°C and 1 atm [1]. The air flow of 40 sccm is the minimum available air flow in the test rig. Figure 4.1 shows the air flow at 40 sccm, the mass flow rate from 350 kg/h and a pressure from 300 mbar. The GVF decreases as the pressure and liquid flow rate increases.

[1] 1 sccm$\approx 1.67 \cdot 10^{-8} \mathrm{m}^3/\mathrm{s}$

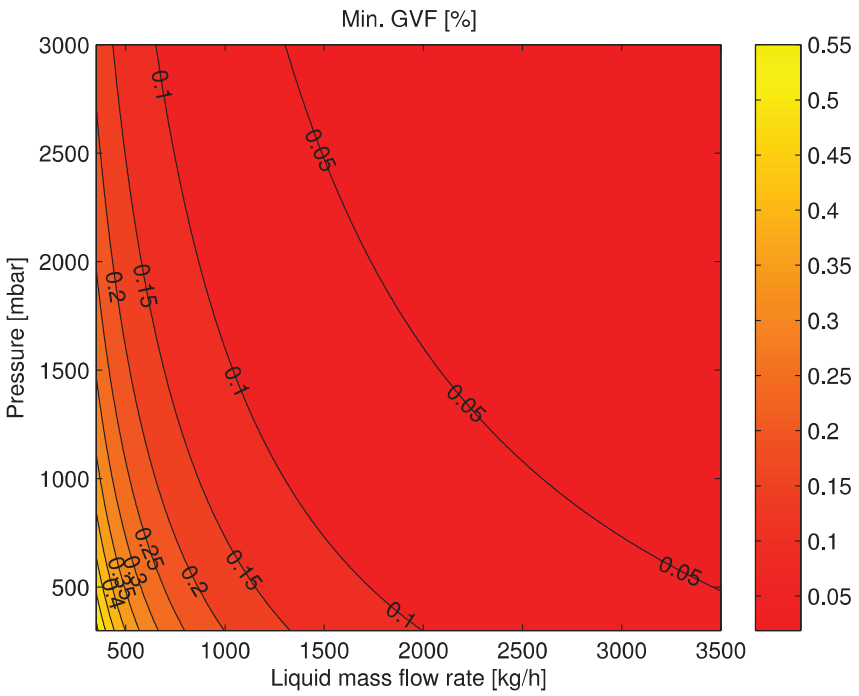

Figure 4.1: The minimum GVF in a fluid at a certain pressure and liquid mass flow rate

It is clear from Figure 4.1 that the liquid flow rate has an impact on the GVF whereas the pressure only have an insignificant impact on the GVF.

The mesh is designed with consideration to "Best practice guidelines" by [ERCOFTAC, 2000]. The guidelines are limited to single-phase, compressible and incompressible, steady and unsteady, turbulence and laminar flow with and without heat transfer. The guidelines do not cover two-phase flow and other complex flow behaviours.
A design practice for two-phase flow in a complex geometry has not been found in the literature search, so the mesh design is based on the well defined and proven guidelines for single-phase flow. See Appendix E for more information on CFD and near-wall modelling.

The turbulence model chosen for the Coriolis flowmeter geometry is the SST k-ω model. This model is distinguished by being good to handle internal flows and flows which exhibit a strong curvature. The SST k-ω model uses the k-ω model near the walls and the k-ϵ model in the free stream. [ANSYS, Inc., 2011]

The geometry with its many bends and curved walls is designed using a hybrid unstructured mesh. The hybrid unstructured mesh have hexahedral and tetrahedral cells. The hexahedral cells are present at the flowsplitter sections. The tube, the inlet and the outlet of the tube have no hexahedral cells. Instead they are modelled with tetrahedral cells. This is deemed, by the author, as the best compromise between the cell number and the computational time.

In order to design the mesh to handle the near-wall modelling approach the y^+-value has to be around 1 or maximum 5. Equation (4.1) finds the mesh spacing between the

wall and the first node away from the wall. Equation (4.2) finds the maximum boundary layer thickness based on the mixture Reynolds number, see Equation (C.11) in Appendix C. The mixture Reynolds number changes as the GVF increases as the liquid flow rate is constant. Figure 4.2 shows how the mixture Reynolds number decreases as the GVF increases. Note that Figure 4.2 is based on a straight pipe section with a liquid flow rate of 3500 kg/h and have no pressure loss across the pipe section.

The pressure has only a significant impact on the compressible gas after a GVF of 10%. The mixture Reynolds number increases more at high pressures than at low pressures. This is caused by the higher pressure giving a higher gas density, which increases the mixture density giving a higher mixture Reynolds number.

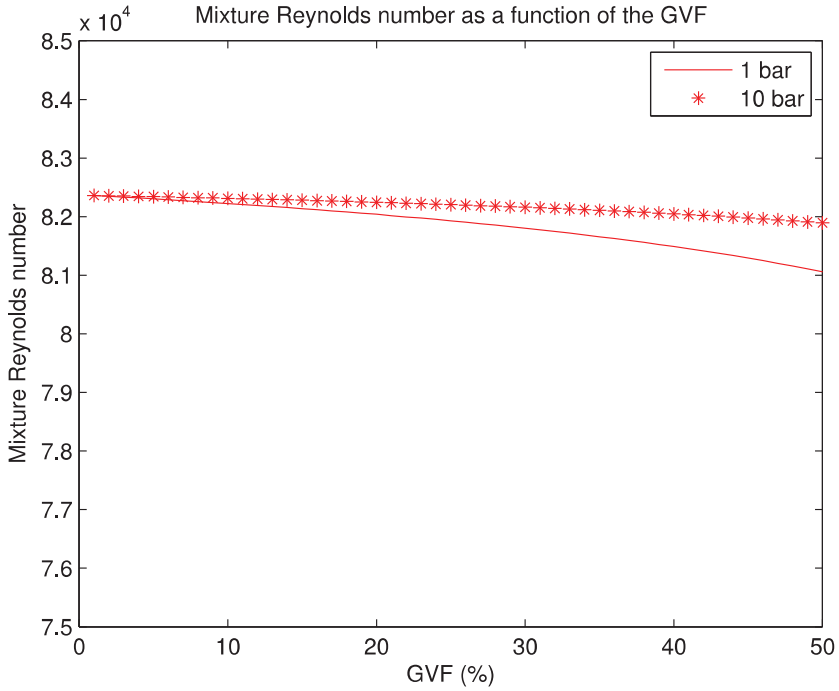

Figure 4.2: Mixture Reynolds number dependent on the GVF and the pressure

The mesh spacing between the wall and the first node away from the wall, Δy_{max} can be found with Equation (4.1) where the y^+-value and the mixture Reynolds number effect the cell height. Equation (4.2) can be used to handle the wall influence and find the maximum boundary layer thickness. The mixture Reynolds number used in the equations are the Reynolds number, with a GVF at zero, in order to create the smallest cell height and boundary layer needed. The equations are derived and cited from [ANSYS, Inc., 2010].

$$\Delta y_{max} = Dy^+ \sqrt{74} Re_{mix}^{-\frac{13}{14}} \tag{4.1}$$

$$\delta_{max} = 0.035 D Re_{mix}^{-\frac{1}{7}} \tag{4.2}$$

In order to have a good representation of the boundary layer minimum 10 cells are needed. δ_{sim} are the boundary layer height in the CFD model, γ is the expansion factor and Δy_{sim}

is the mesh spacing between the wall and the first node away from the wall in the CFD model. [ANSYS, Inc., 2010]

$$\delta_{\text{sim}} = \Delta y_{\text{sim}} \sum_{i=1}^{9} \gamma_{\text{sim}}^{i}$$
$$\delta_{\text{sim}} < \delta_{\text{max}}$$
$$\Delta y_{\text{sim}} < \Delta y_{\text{max}}$$

The mesh will be designed so the boundary layer grid can handle a liquid mass flow of 3500 kg/h, which is the largest mass flow in the experiments. The mesh is designed so that the tube, the inlet and outlet pipe have a 10 cell boundary layer with a y^+-value of 5. Table 4.1 shows the calculated and chosen spacing between the wall and the first node away and the boundary layer height. The δ_{max} for the tube domain is exceed a little but it is only the last cell in the 10 cell boundary layer that exceed the limit. This is deemed acceptable.

Geometry	Inlet/Outlet	Tube
Re_{max}	71410	82360
Δy_{max}	0.0463 mm	0.0176 mm
Δy_{sim}	0.0106 mm	0.0045 mm
δ_{max}	0.1227 mm	0.0521 mm
δ_{sim}	0.1227 mm	0.0531 mm

Table 4.1: Mesh design with a y^+-value of 5 and $\gamma_{\text{sim}} = 1.05$

The mesh designed will have the boundary layer settings mentioned in Table 4.1. The mesh is designed so the curved part of the domain has smaller and more cells than the non-curved part of the domain. The mesh will have a velocity inlet and a pressure outlet.

4.2 Grid Independence

The transient two-phase fluid CFD simulation to simulate the fluid behaviour through the flowmeter needs a mesh, which is grid independent. A higher cell number in a mesh increases the computational time. A grid convergence study is performed in Section 4.2.1 in order to evaluate the three designed meshes. The designed meshes will have the same boundary layer resolution, but will vary in the rest of the domain in cell number. The three designed meshes have 152356, 357934 and 632376 cells, respectively.

In order to simplify and reduce computation time the grid convergence study is performed for a single-phase liquid water flow at 20°C at 1 m/s with a specified back-pressure at 300 mbar in steady state. The meshed domain is solved using ANSYS FLUENT 14.0. Table 4.2 shows the settings for the steady state cases.

Steady state settings	
Solver	Pressure based
Turbulence model	k-ω SST
Inlet boundary conditions	Velocity inlet 1 m/s
Outlet boundary conditions	Pressure outlet 30000 Pa gauge pressure
Discretization scheme	Second order upwind
Solution algorithm	SIMPLE
Gravity in y-direction	9.81 m/s^2
Material	Water, ρ=998.2 kg/m^3 - incompressible

Table 4.2: FLUENT settings for the steady state case

Appendix F contains the cell information for the three meshes along with the steady state residual plots and tables with quality indicators as skewness and orthogonal quality. The steady state solution is deemed converged when the scaled residuals (see Appendix F) are below 10^{-3} and no visible changes occur.

4.2.1 Grid Convergence Study

A grid refinement study is needed to provide a measure of uncertainty of the grid convergence. A grid refinement study requires a series of grid refinements to assess the effect of grid resolution. As the grid is refined (cell number in the domain increases) the spatial discretization error should asymptotically approach zero, disregarding computer round off error. [Slater, 2008]

The Grid Convergence Index, GCI method suggested by P. J. Roache provides a consistent manner in reporting and evaluating the results of grid convergence studies. The GCI is based upon a grid refinement error estimator derived from the theory of generalized Richardson's Extrapolation. Richardson's Extrapolation is used to calculate a higher-order estimate of the flow fields from a series of lower-order solutions (ϕ_1, ϕ_2,...,ϕ_k,..., ϕ_n). The generalization of Richardson's Extrapolation lies in introducing the p$^{\text{th}}$-order methods, see Equation (4.3) [Ali et al., 2009]. Here r is the grid refinement ratio. The indices in Equation (4.3) denote the steps in the solution *e.g.* $\phi_{i,j}$=$\phi_{k,0}$ means j=0 is the first solution with mesh i=k.

$$\phi_{k,1} = \phi_{k,0} + \frac{\phi_{k,1} - \phi_{k-1,0}}{r^p - 1} \tag{4.3}$$

Using a second order scheme then the first two results will have an order of accuracy of O(h^2) and halving the step size, will give the standard fourth order Richardson extrapolation formula (4.4). [Lund and Condra, 2013]

$$\phi_{k,1} = \frac{4\phi_{k,0} - \phi_{k-1,0}}{3} \tag{4.4}$$

[Celik, 2003] recommends a procedure for estimation of discretization errors for finding the GCI for a set of grids.

The comparison will be over three grids with the area-weighted pressure loss between the inlet and outlet of the flowmeter as the solution variable ϕ_i, see Table 4.3. h_i is the cell numbers in each of the three grids.

Grid, i	Cell number, h_i	ΔP (Pa), ϕ_i
1	152356	6475.52
2	357934	6314.77
3	632376	6305.53

Table 4.3: Grid data

Let $h_1<h_2<h_3$ and $r_{21}=h_2/h_1$, $r_{32}=h_3/h_2$. The apparent order, p of the method can be calculated using Equation (4.5).

$$p = \frac{1}{ln\left(r_{21}\right)}\left|ln\left|\frac{\epsilon_{32}}{\epsilon_{21}}\right| + q(p)\right| \tag{4.5}$$
$$q(p) = ln\left(\frac{r_{21}^p - s}{r_{32}^p - s}\right)$$
$$s = 1 \cdot \text{sign}\left(\frac{\epsilon_{32}}{\epsilon_{21}}\right)$$

where $\epsilon_{32}=\phi_3$-ϕ_2 and $\epsilon_{21}=\phi_2$-ϕ_1. Equation (4.5) solution can be found iteratively. Note that q(p)=0 when r is constant.

According to [Slater, 2008] the theoretical order of convergence is p=2.0, where the actual p is 2.37 as seen in Table 4.4. The difference is most likely due to grid stretching, grid quality, turbulence modelling and perhaps other factors.

Equation (4.6) and (4.6) find the approximately relative errors. Equation (4.8) and (4.9) find the GCI in percentage. The GCI value represents the resolution level and how much the solution approaches the asymptotic value [Ali et al., 2009].

$$e_{a21} = \left|\frac{\phi_1 - \phi_2}{\phi_1}\right| \tag{4.6}$$
$$e_{a32} = \left|\frac{\phi_2 - \phi_3}{\phi_2}\right| \tag{4.7}$$
$$\text{GCI}_{21} = \frac{F_s e_{a21}}{r_{21}^p - 1} \cdot 100 \tag{4.8}$$
$$\text{GCI}_{32} = \frac{F_s e_{a32}}{r_{32}^p - 1} \cdot 100 \tag{4.9}$$

F_s is a factor of safety of 1.25. GCI_{21} is the GCI for grid 1 and 2. GCI_{32} is the GCI for grid 2 and 3.

A check to see if the solutions are in the asymptotic range of convergence is performed in Equation (4.10).

$$\text{Ratio} = \frac{\text{GCI}_{21}}{r_{21}^p \text{GCI}_{32}} \tag{4.10}$$

A ratio of 1% indicates that the solutions are within the asymptotic range of convergence. [Slater, 2008]

Table 4.4 contains the results from the grid convergence analysis.

Variable	Value
p	2.3684
GCI_{21}	0.4730%
GCI_{32}	0.0642%
Ratio	0.9752%

Table 4.4: Grid convergence results

In Table 4.4 the ratio of approximately 1% indicates that the solutions are in the asymptotic range of convergence. The low GCI means that a further refinement of the grid will not give much change in the simulation results.

4.3 Final Mesh Design

The mesh with 152356 cells is the mesh used in the simulations, since the GCI analysis reveals that a mesh with a finer divided domain will not change the simulation results significantly. The mesh with 152356 cells can be seen in Figure 4.3. The flowdirection is from left to right.

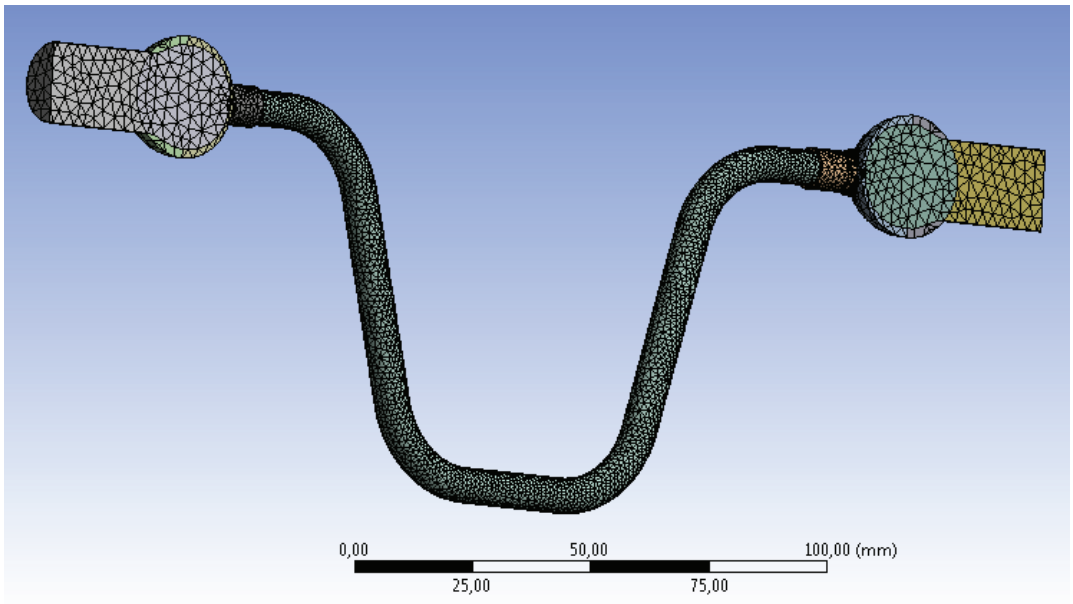

Figure 4.3: The meshed domain

Some of the interesting parts of Figure 4.3 can be seen in Figure 4.4.

Figure 4.4a and 4.4b shows the meshed domain at the inlet and flowsplitter. The boundary layer grid can be seen in the inlet section close to the wall in Figure 4.4c. From the flowsplitter to the tube there are a higher amount of cells which are smaller than in the rest of the domain due to the curved domain.

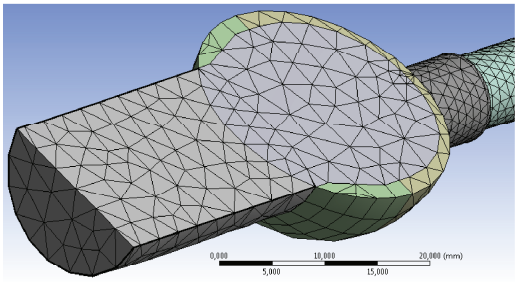

(a) Inlet section with boundary layer grid

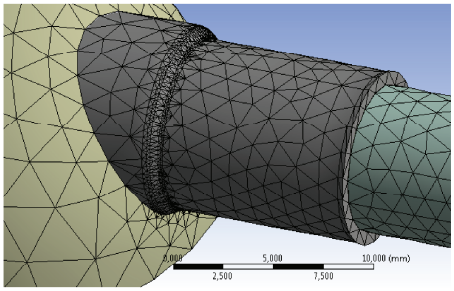

(b) The finer grid in the flowsplitter

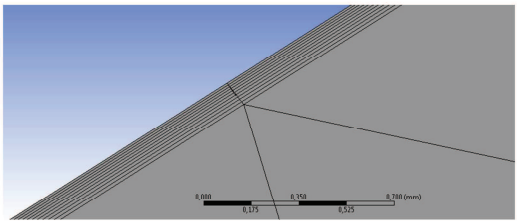

(c) Boundary layer grid close up

Figure 4.4: Specific parts of the mesh

Aerated flow simulations will be performed with the final mesh design in Chapter 5 to investigate the two-phase flow behaviour in the SITRANS FC400 sensor.

Chapter 5

Simulations of flow behaviour in FC400 sensor

The flow behaviour will be investigated through a series of parametric studies. In analysing the Coriolis flowmeter the 152356 cells mesh is deemed suited with the use of GCI. In order to see the fluid behaviour and the influence the bubbles have on this, three cases will be evaluated.

- Steady single-phase liquid flow through the flowmeter
- Transient single-phase liquid flow through the flowmeter
- Transient two-phase fluid flow through the flowmeter

The author hypothesizes is that there will be no significant change between the two single-phase cases. The three cases will be examined with the same settings except for the steady/transient option and the amount of air in the system.

5.1 Simulation Parameters

The CFD calculations performed in FLUENT are set to use the mixture model, which is a simplified multiphase model that can be used to model multiphase flows where the phases move with different speeds. The mixture model is designed to handle multiphase modelling. The mixture model can be used when having bubbly flows where the GVF is low and homogeneous multiphase flows. It has limitations though, only one phase can be defined as a compressible gas. [ANSYS, Inc., 2011]

The mixture model solves the continuity equation (5.1) for the mixture, where the velocity $\vec{U}_{\text{mix}}$ is based on the volume fraction of phase i.

$$\frac{\partial}{\partial t}\left(\rho_{\text{mix}}\right) + \nabla\left(\rho_{mix}\vec{U}_{\text{mix}}\right) = 0 \tag{5.1}$$

$$\vec{U}_{\text{mix}} = \frac{\sum_{i=1}^{n} \epsilon_i \rho_i \vec{U}_i}{\rho_{\text{mix}}}$$

The slip velocity is activated under the mixture model. FLUENT will then compute the phases with different speed. [ANSYS, Inc., 2011]

A more detailed explanation and equations for the models can be found in the extensive documentation provided by ANSYS and will not be reproduced here.

The 152356 cells domain is solved using ANSYS FLUENT 14.0. Table 5.1 shows the settings for the cases. The fluid into the flowmeter is dispersed bubble flow with bubbles with a diameter of 1 μm, which is the default setting.

Fluent settings	
Solvers	Pressure based
Model	Mixture model with slip velocity
Turbulence model	k-ω SST
Inlet boundary conditions	Mass flow inlet
Outlet boundary conditions	Pressure outlet
Discretization scheme	Second order upwind
Solution algorithm	SIMPLE
Gravity in y-direction	-9.81 m/s^2
Material	Water and air at 20°C - incompressible

Table 5.1: FLUENT settings for the cases

The inlet is a mass flow inlet. The mass flow for the air and the water can be specified individually. The inlet velocity profile is straight since no knowledge of the velocity profile is known. The GVF will be changed in the transient setup as seen in Table 5.2.

Case	GVF
1	0%
2	5%
3	10%

Table 5.2: GVF inlet boundary conditions

The simulation will be run transiently in order to see the flow regime and the fluid behaviour. The travel time, t for a bubble through the meter depends to a great extent on the liquid flow rate and the length the bubble will have to travel Δx from the inlet to the outlet. The travel time can be roughly estimated as seen in Equation (5.2). In order to simplify the analysis some crude assumptions are used. The liquid density and the liquid mass flow is assumed to be the mixture density and mass flow. The travel length is longer than the Δx mentioned in Table 5.3, but the precise travel length is unknown. The smaller travel length gives a shorter travel time.

$$t = \frac{\Delta x}{U_{\max}} \tag{5.2}$$
$$U_{\max} \approx \frac{\dot{m}_l}{\rho_l A}$$

The maximum fluid speed U_{max} changes for the different simulation cases which changes the travel time. The simulations with the largest velocities will have the need for the smallest timestep in order to see the fluid behaviour.

Parameters	Value
A_{inlet}	$2.351 \cdot 10^{-4}$ m^2
ρ_l	998.2 kg/m^3
m_l - Min	350kg/h
m_l - Max	3500 kg/h
Δx	0.26687 m
t - Min	0.642 s
t - Max	0.064 s

Table 5.3: Values for the timestep analysis. Min and Max refers to the minimum and maximum liquid flow rate

The travel time for the minimum and maximum liquid flow rate are 0.642 s and 0.064 s. A resolution of the solution at 100 steps gives a timestep size of $6.42 \cdot 10^{-3}$ s and $6.42 \cdot 10^{-4}$ s respectively.

During the simulations the timestep size changes. The first iterations will have a smaller timestep size in order to obtain convergence in the beginning of the simulation. The timestep size will then be increased slowly as the simulation progresses. The step size will not be increased above the before mentioned size of $6.42 \cdot 10^{-3}$ s and $6.42 \cdot 10^{-4}$ s for the minimum and maximum liquid flow rate.
Each timestep will have several iterations in order to obtain convergence for the timestep.

5.2 Case Studies

The simulation results of the three cases will be summarized in the following sections. The simulations will have the parameters and model settings as described in Section 5.1. The y^+-value and contour plots of the speed will be used as solution evaluating parameters. The hypothesis mentioned in the start of this chapter will be investigated.

Figure 5.1 shows where the planes are located. Contour plots of the speed will be made on these cross section plane locations and be used to compare the steady and transient single phase simulations. The cross section planes are located to see the behaviour of the fluid in two different settings. Plane 1 is in the straight section of the tube. The speed of the fluid should be strongest in the middle of the tube due to the development of the flow. Plane 2 is is located at the end of the tube. The highest speed of the fluid will not be located in the centre due to the bend the flow has just experienced and the enlargement of the cross section area, see Table 5.4.

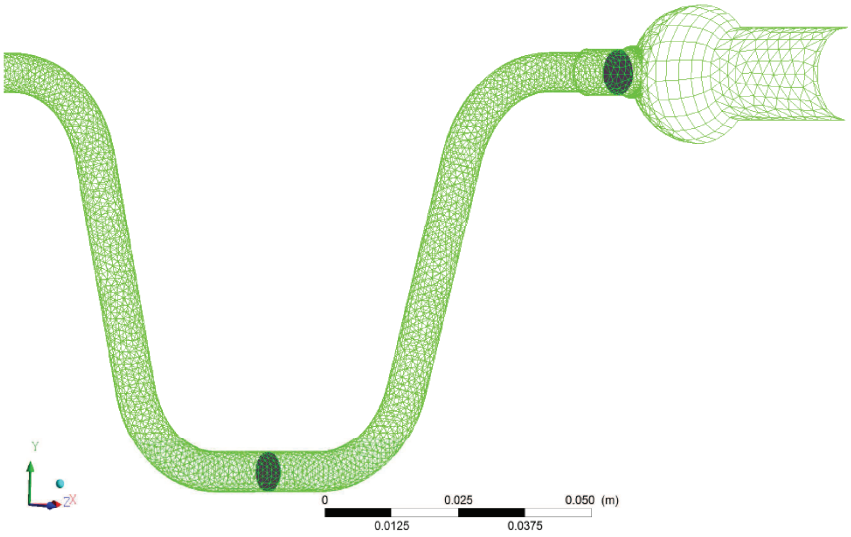

Figure 5.1: Positions of cross section planes. Inlet to the left and outlet to the right

Table 5.4 lists the cross section plane locations and their area. The locations are defined as the horizontal length from the inlet. The outlet of the Coriolis flowmeter is located 266.87 mm horizontal from the inlet, see Appendix I for further information on the geometry.

	Horizontal length from inlet	Area
Plane 1	133.4 mm	43.30 mm^2
Plane 2	215.9 mm	58.79 mm^2

Table 5.4: Locations and area of the cross section planes

The simulations are expected to show recirculation zones in the flowsplitters due to the expansion of the diameter and the dividing/collecting of flow streams. In the tube the flow is expected to be effected by the bends. Paraphrasing [Munson et al., 2010]; “pipe

bends produce a greater pressure loss than if the pipe was straight. The losses are due the separation region of flow near the inside of the bend." The pressure is expected to be high at the outside of the pipe and decreasing inwards towards the inside of the bends, which gives a opposite velocity gradient.

5.2.1 Steady Single-Phase Liquid Flow Through the Flowmeter

The steady single-phase simulation is set up as a base case with a liquid flow rate of 350 kg/h. The base case simulation will evaluate the mesh based on the y^+-value. The residual plot can be found in Appendix G in Figure G.1.

The mesh was designed to handle the highest mixture Reynolds number and have a y^+-value of 5 in the inlet, tube and outlet. Figure 5.2 shows the y^+-value as a function of the x-axis through the Coriolis flowmeter. The y^+-value after a steady single-phase simulation is low at the designed sections. The y^+-value is lower in the inlet, tube and outlet sections than the designed value of 5. This is caused by the lower liquid flow rate in the simulation than the design liquid flow rate of 3500 kg/h.
Interestingly the highest y^+-value is just below 60 which is in the flowsplitters. A y^+-value of 60 is relatively low since there where no special boundary layer grid design considerations at the flowsplitters. The curvature in the domain, where there was a refinement of the grid, has solved the wall influence acceptably.

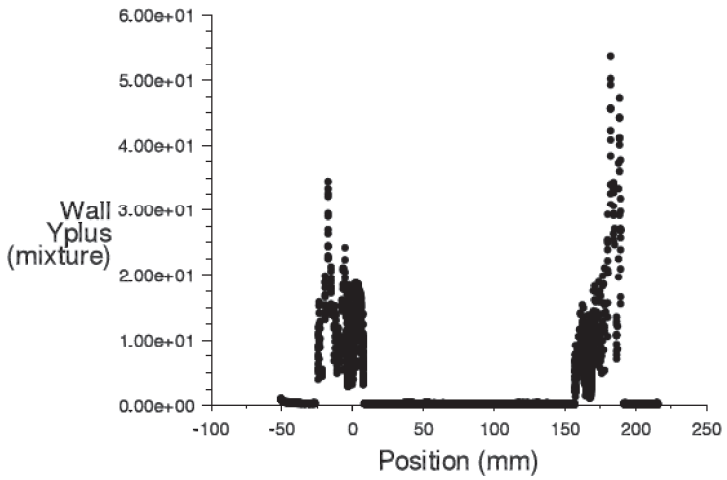

Figure 5.2: y^+-value for the steady simulation with a liquid flow rate of 350 kg/h

The y^+-value is important since the near-wall features are of interest. If the Reynolds number is low, the viscous effect near the wall has a bigger impact and near wall modelling is needed. In order to solve the viscous layer accurately the y^+-value needs to be around 1. [ANSYS, Inc., 2006]

Figure 5.3 shows the contour plot of the speed of the fluid. At the left side is the inlet, then comes the first flowsplitter, the tube, the second flowsplitter and then at the right side is the outlet of the flowmeter. Note that only the inlet, flowsplitters and outlet gives an insight into the fluid behaviour, since the contour of the tube is only the speed of the

fluid at the wall. Recirculation zones can be seen at the tube outlet in the flowsplitter. The recirculation zones causes the speed of the fluid at the outlet of the flowmeter to have a non-uniform velocity profile.

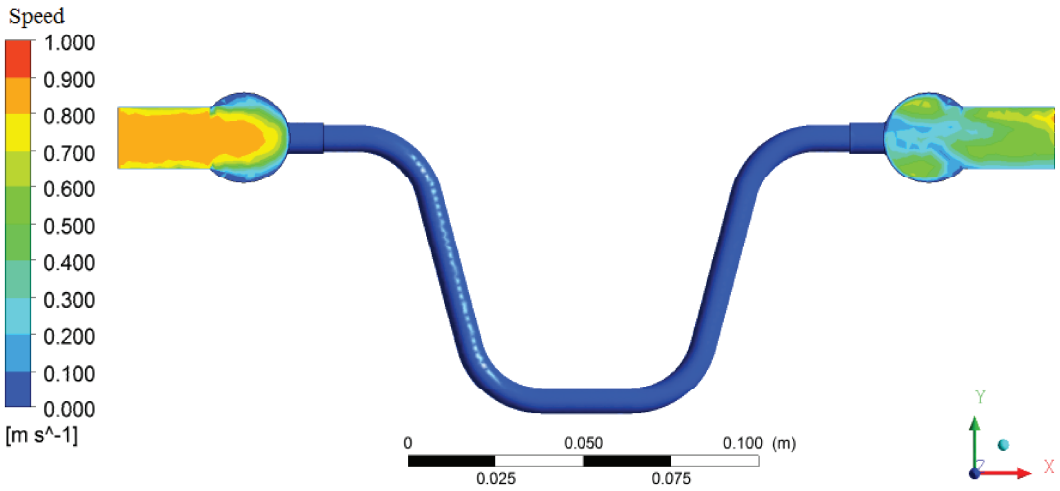

Figure 5.3: Contour plot of the speed of the fluid in the flowmeter. The contour of the tube is only the speed of the fluid at the wall

Figure 5.4 and 5.5 are vector plots describing the velocity of the fluid at the symmetry plane of the inlet, outlet and flowsplitters. The colour of the vectors define the x-velocity and the direction of the arrows the general fluid behaviour. The recirculation zones can be identified by the negative x-velocities at the top and bottom of the flowsplitters.

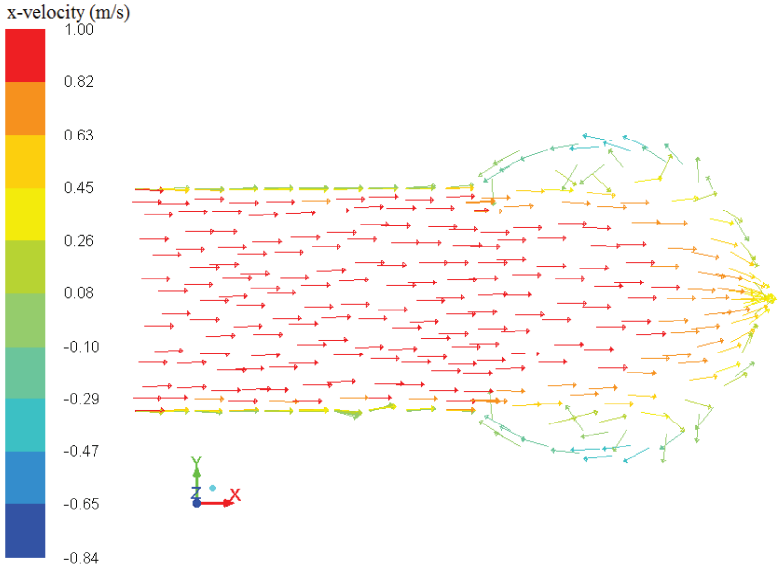

Figure 5.4: Steady single-phase vector plot of the x-velocity in the symmetry plane of the inlet part of the Coriolis flowmeter

The green vectors indicate a zero x-velocity at the walls of the inlet and outlet sections. At the flowsplitter in the outlet section it can be seen on the velocity vectors, that the

tube is located behind the symmetry plane.

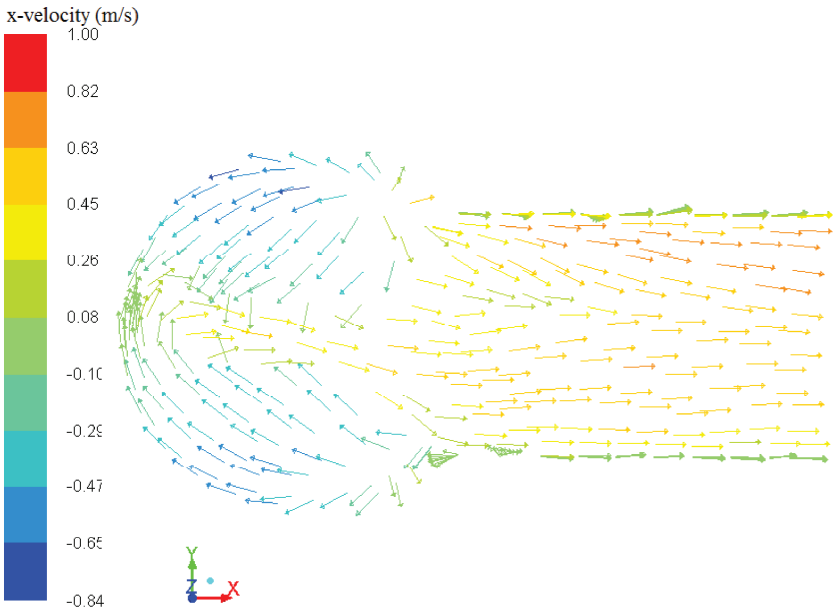

Figure 5.5: Steady single-phase vector plot of the x-velocity in the symmetry plane of the outlet part of the Coriolis flowmeter

In Figure 5.6 two contour plots of the velocity at Plane 1 and Plane 2 are seen.

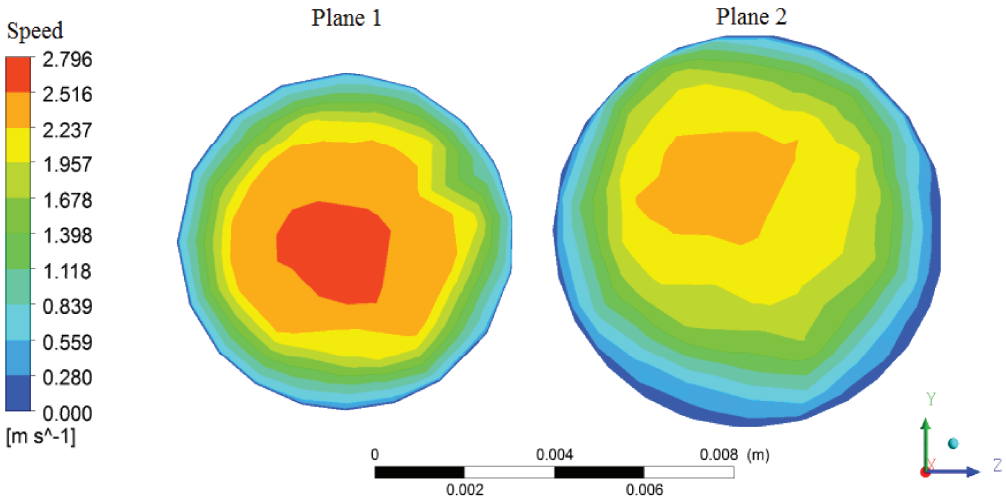

Figure 5.6: Steady single-phase liquid flow case, contour plot

At Plane 1 the velocity is zero at the walls as expected and increases as the centre of the pipe is reached. The contour plot does not show completely uniform velocity circles since the flow is recovering from the previous bending of the tube.

The velocity contour plot of Plane 2 shows a general lower velocity over the entire cross section, this is caused by the larger area of Plane 2 compared to Plane 1. The highest speed is offset from the centre of the tube due to previous bending of the tube.

5.2.2 Transient Single-Phase Liquid Flow Through the Flowmeter

The transient single-phase is compared to the steady single-phase case in order to see if and when a steady state enters the simulation, therefore the liquid flow rate is the same. Three contour plots showing the speed development over 1.5 s for the symmetry part of the domain can be seen in Figure 5.7. Between 0.125 s and 0.5 s the flow speed contours change, especially at the outlet. There is no significant change after 0.5 s. It can hereby be assumed that the steady state occurs before or at 0.5 s. This time is close to the estimated travel time in Section 5.1 and proves that the estimated travel time can be used to estimate the required simulation time to see the flow behaviour.

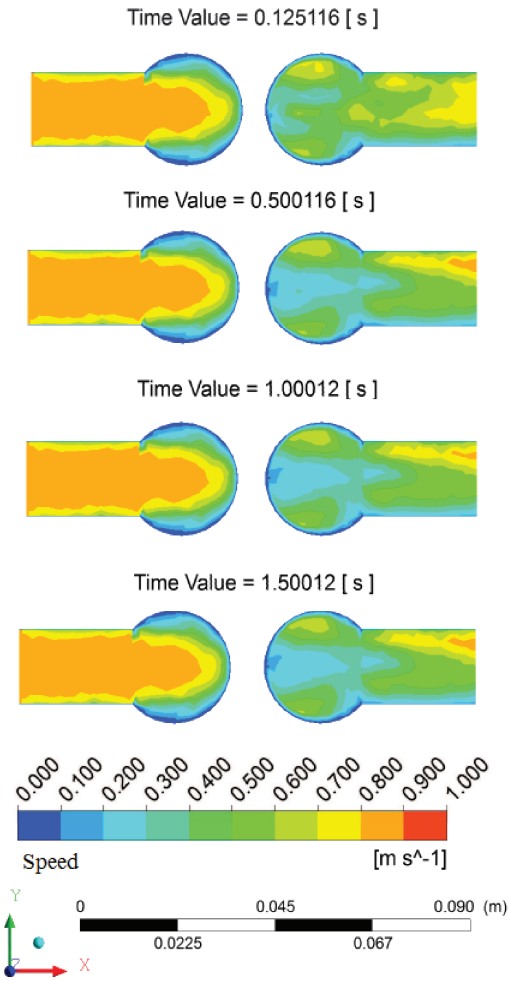

Figure 5.7: Transient single-phase liquid flow case, contour plot of the flow speed

The cross section planes seen in Figure 5.8 are similar to the flow speed plots for the steady single-phase case, see Figure 5.6. The transient single-phase flow behaviour regarding the speed have the same tendencies as the steady single-phase flow.

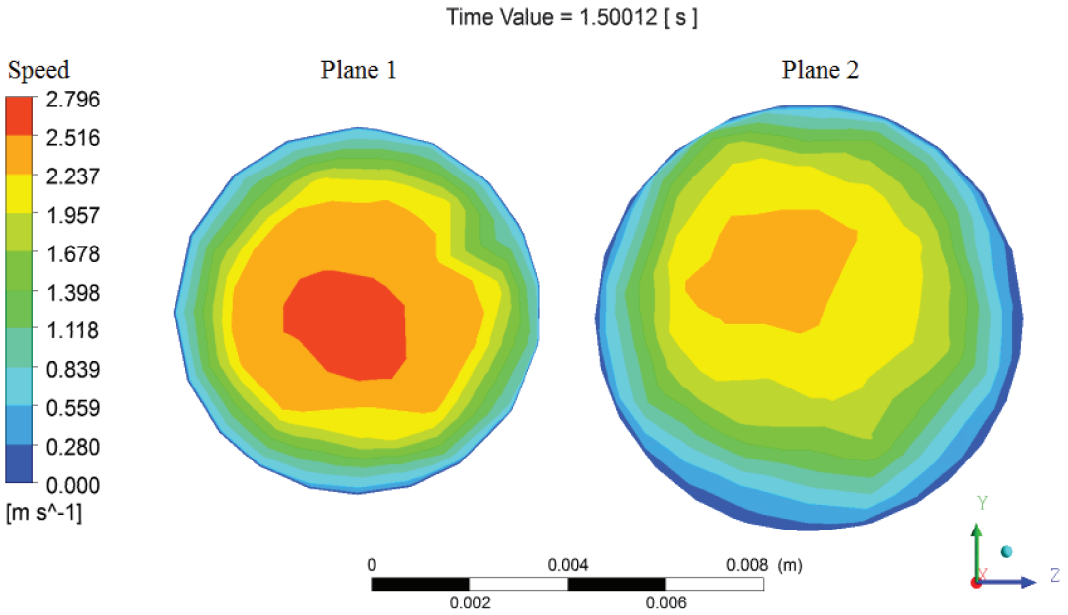

Figure 5.8: Transient single-phase liquid flow case, contour plot of the flow speed

Figure 5.9 shows the centre plane of the tube. The speed of the flow is high at the inside of a bends. After the bends the fluid is shifted to the outside of the tube. This is caused by the pressure gradients at the bends and the recirculation zones at the inside of the tube after the bends.

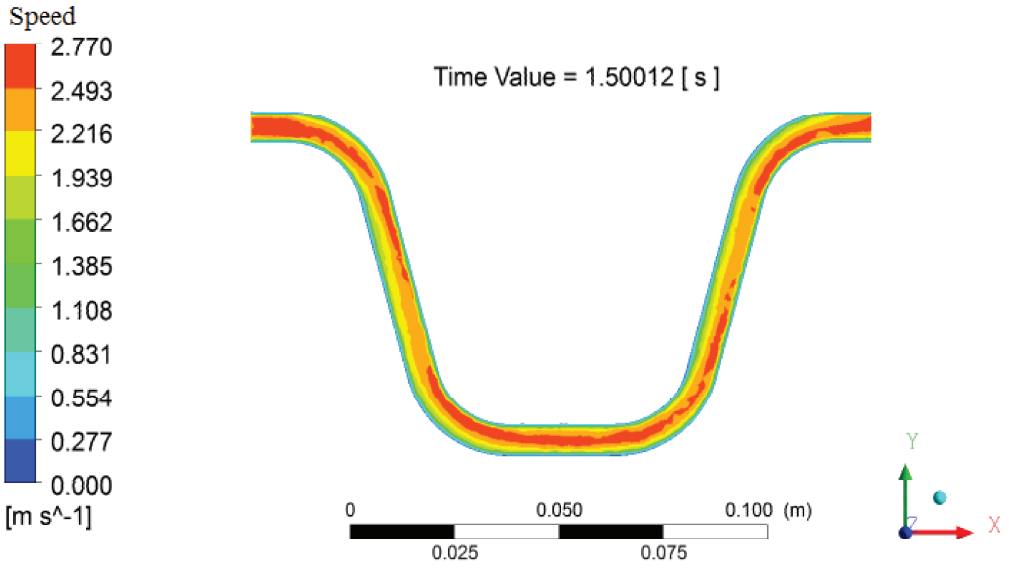

Figure 5.9: Centre plane of the tube, contour plot of the flow speed

There is no significant change between the steady and transient single-phase flow solutions. The steady single-phase solution is chosen as the initial guess to the transient two-phase flow simulation.

5.2.3 Transient Two-Phase Fluid Flow Through the Flowmeter

The steady single-phase solution is the initial guess when the gas is introduced. Three simulations with varying inlet parameters and one constant outlet parameter are investigated, see Table 5.5.

Liquid flow rate (kg/h)	GVF (%)	Back-pressure (mbar)
350	5	300
3500	5	300
350	10	300

Table 5.5: Boundary conditions

Excerpts from residual plot for the transient two-phase cases can be found in Appendix G. The video of the simulations can be found in Appendix A.1 for further investigation.

Liquid Flow Rate of 350 kg/h with 5% GVF

Figure 5.10 shows the behaviour of the flow 0.11 s after the gas enters at time t=0. The air volume fraction is highest where the local velocity components are largest, see the flow speed contour plot Figure 5.9 for transient single-phase flow.

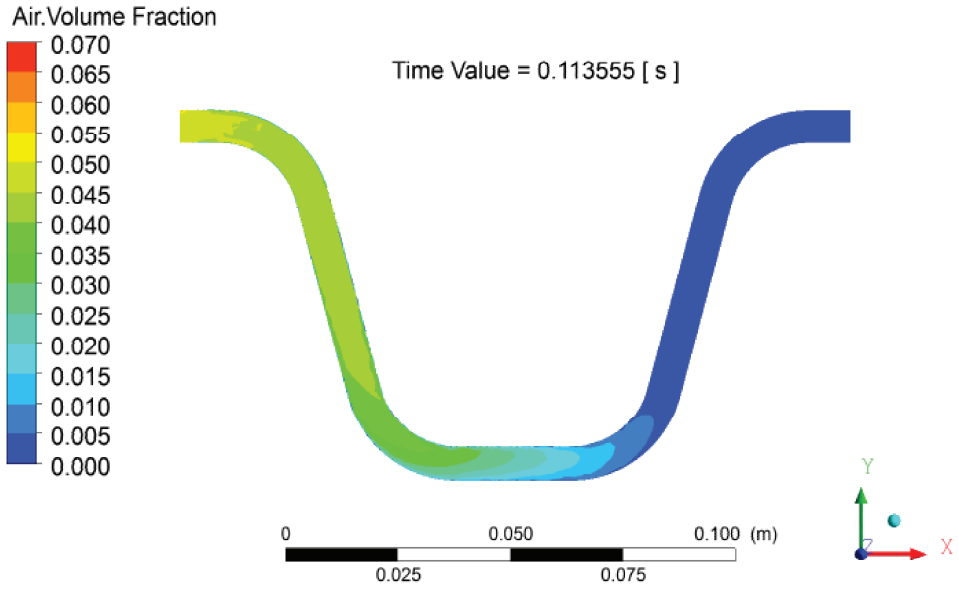

Figure 5.10: Contour plot of the air volume fraction in the centre plane of the tube after 0.11 s

The flow become stable after approximately 0.8 s, which is close to the crude estimation of the travel time made earlier. The highest amount of gas lies in the same area as where the flow speed for the transient single-phase case was high. The arrows on Figure 5.11

shows the areas where the gas volume fraction is higher than the GVF sent in. These areas are named Gas Volume Fraction Areas, GVFA in the rest of the report.

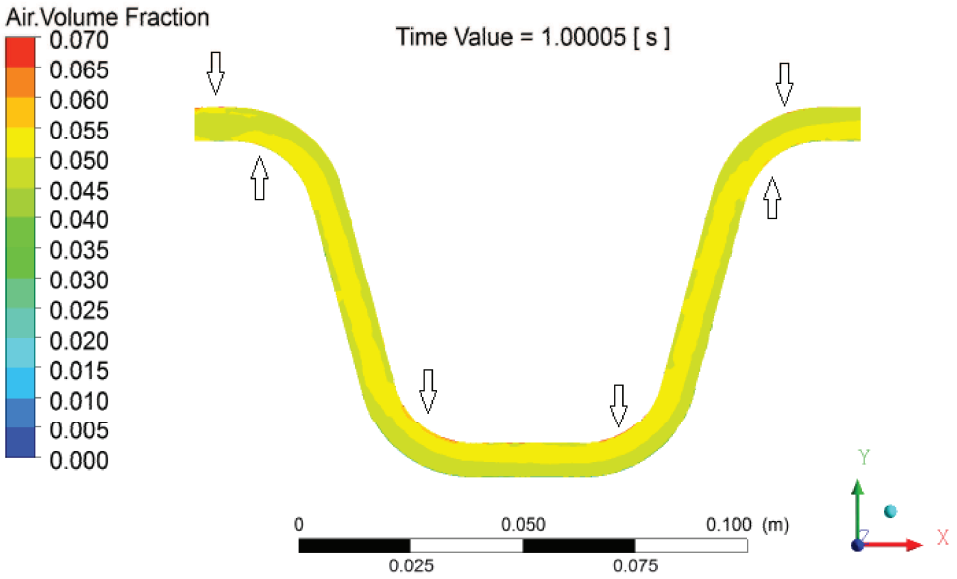

Figure 5.11: Contour plot of the air volume fraction in the centre plane of the tube after 1 s. The arrows indicate the location of the GVFA

Rotating the simulated domain shows the areas with the higher gas fraction over the entire domain. The GVFA lies close to the tube wall. In the rest of the domain where the GVFA are not present, the gas fraction is approximately constant over the tube cross section. The location of the GVFA follows the theory, that the gas volume fraction will be high, where the flow has a high speed and where the pressure is low through the flowmeter.

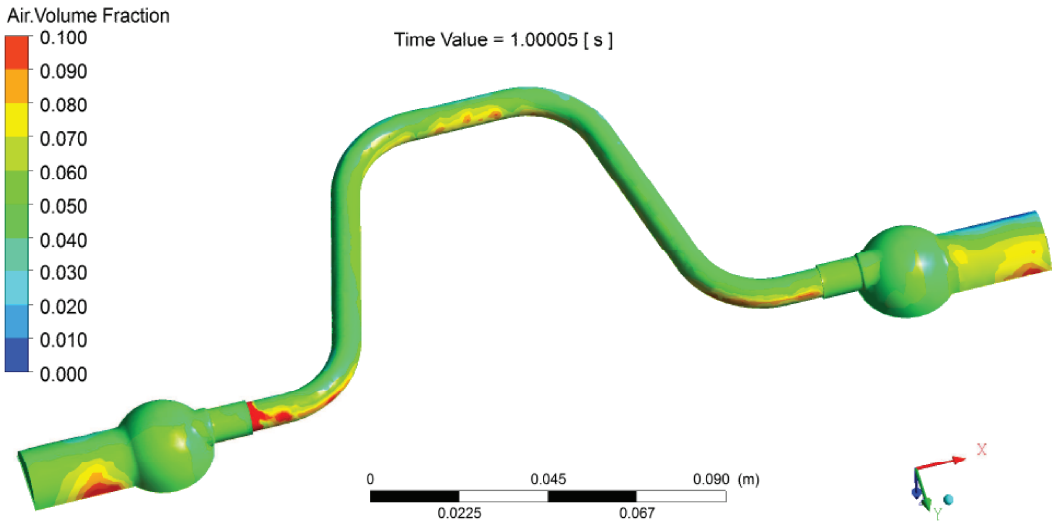

Figure 5.12: Contour plot of the air volume fraction after 1 s. Note the domain is rotated

Liquid Flow Rate of 3500 kg/h with 5% GVF

The experiment showed that for the FC430 Coriolis flowmeter the measurement errors for both the mass flow rate and the density increases as the GVF increases. The measurement errors for the density increases when the liquid flow rate increases. The knowledge of the liquid flow rate increase influence on the measurement errors, will be tested with a simulation where the liquid flow rate is increased and the GVF is kept constant. The transient two-phase flow case 0.26 s after the air enters the flowmeter can be seen in Figure 5.13 and 5.14. Increasing the liquid flow rate in the simulation shows that the GVFA increases but stay at the same location.

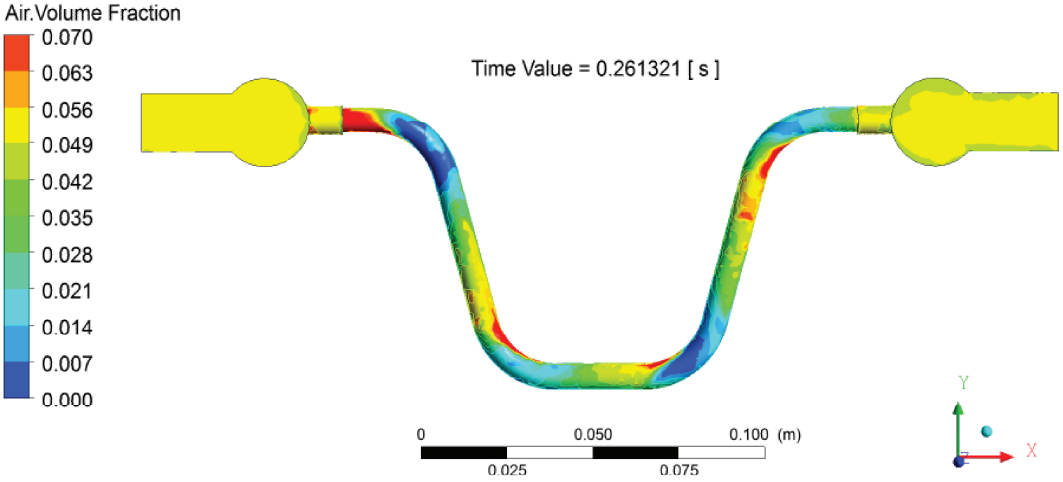

Figure 5.13: Contour plot of the air volume fraction in the domain after 0.26 s

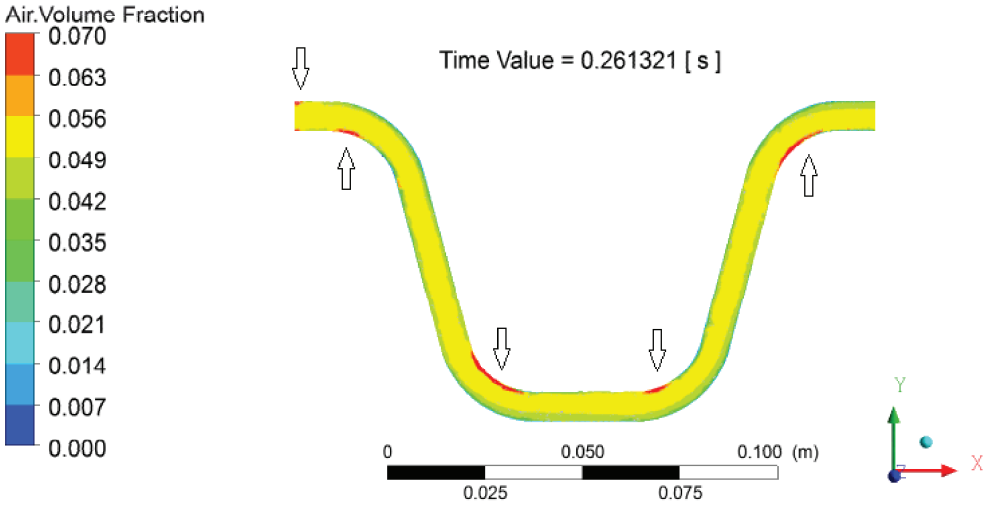

Figure 5.14: Contour plot of the air volume fraction in the centre plane of the tube after 0.26 s. The arrows indicate the location of the GVFA

The gas fraction areas are separated at the bottom of the tube. The centre of gravity through the tube will be different for the 350 kg/h and 3500 kg/h liquid flow rates, even

through they have the same gas volume fraction at the inlet. The increase of liquid flow rate increases the decoupling error. See Section 1.1 for more information on the centre of gravity and the decoupling error.

Liquid Flow Rate of 350 kg/h with 10% GVF

As mentioned in the previous section the experiment showed an increase in measurement errors as the GVF increased. A liquid flow rate of 350 kg/h and a 10% GVF as inlet boundary conditions give similar results compared to the other simulations. The air fraction areas are increased when comparing the results (Figure 5.15) with the other transient two-phase simulations. In the bottom of the tube the areas are no longer separated. At the inlet section of the tube the air volume fraction is increases.

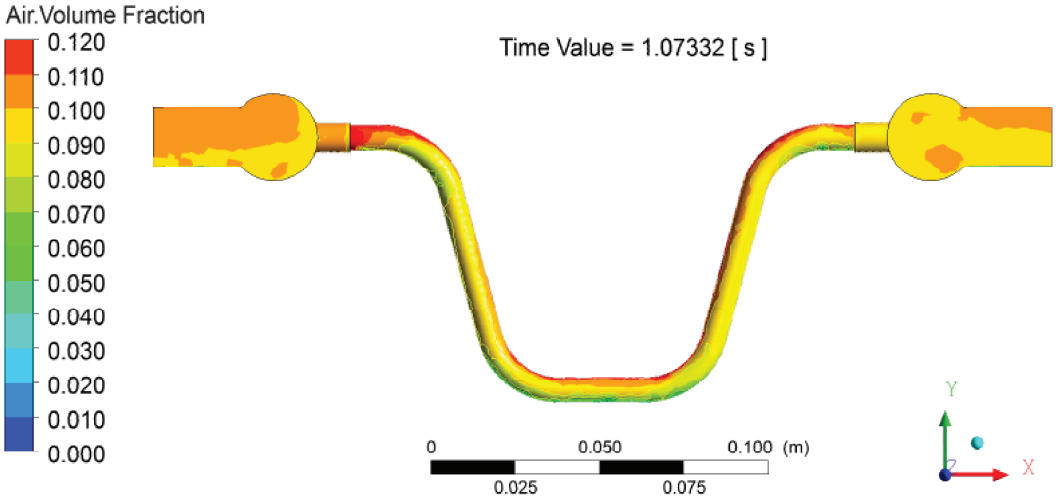

Figure 5.15: Contour plot of the air volume fraction after 1 s

Figure 5.15 showing the wall of the tube shows that only the inner curve of the tube has GVFA at the wall. Figure 5.16 shows that the higher air volume fraction continues to lie in the same “track” as seen in the other simulations.

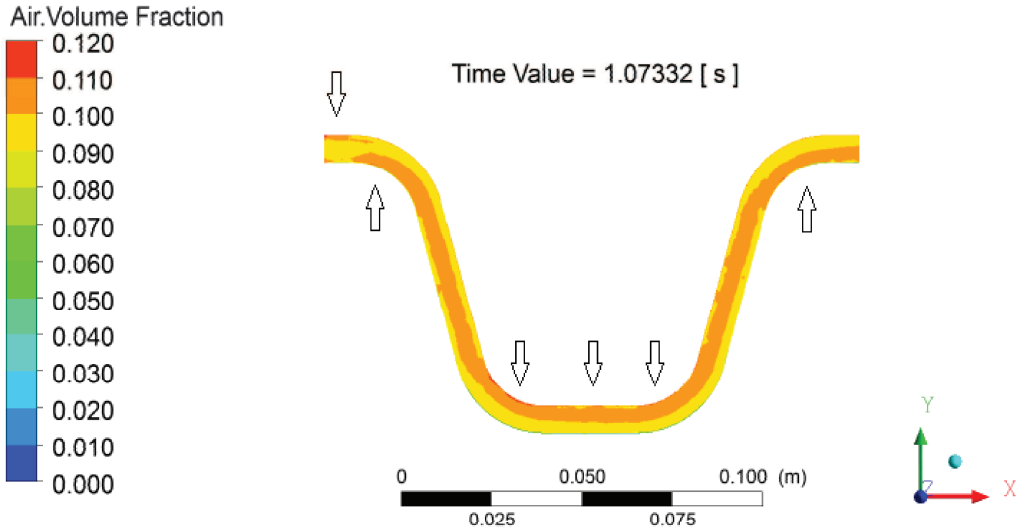

Figure 5.16: Contour plot of the air volume fraction in the centre plane of the tube after 1 s. The arrows indicate the location of the GVFA

Examining Figure 5.17 shows that the GVFA lies only at the inner curve of the tube and that large GVFA occurs at the inlet and outlet of the flowmeter.

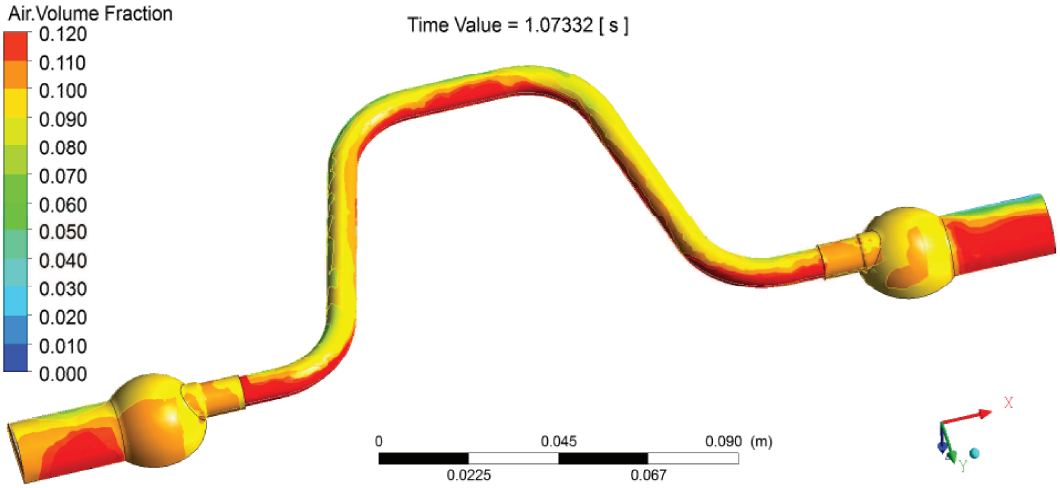

Figure 5.17: Contour plot of the air volume fraction after 1 s. Note the domain is rotated

There is a significant difference when comparing Figure 5.12 and Figure 5.17 to the size of the GVFA even though there is only a 5% GVF difference between the two simulations. A further increase in GVF would cause larger GVFA than seen in Figure 5.17 which would cause a larger decoupling effect. This observation fits well with the general observation that at large GVF the Coriolis flowmeter will fail to function properly.

5.2.4 Summary of the Simulations

The flow in the Coriolis flowmeters becomes steady shortly after the estimated travel time. The experimental data is collected 15 s after the air enters the water, which means that the air has spread through the entire flowmeter when the fluid properties are measured in the experiments.
The simulations showed that the phases do not have the same velocity since areas of larger gas fractions are located. During the simulations the areas with larger gas fractions do not change after the flow becomes stable. The GVFA could become unstable but further simulation are required in order to investigate this.

The GVFA have a higher gas volume fraction than the inlet boundary condition, which leads to other areas of the flowmeter to have a low air volume fraction. The GVFA are located where the velocity is high and in the bend where the pressure is low. Changing the inlet boundary conditions to a higher liquid flow rate and keeping the same GVF leads to an increase of the GVFA. The GVFA at the bottom of the tube is separated and lies at each bend.

The large measurement errors for the density seen in the experiment when the liquid flow rate is increased and that the GVF is constant, fits well with the theory of decoupling and the increased GVFA. Increasing the GVF and keeping the liquid flow rate constant increases the measurement errors for both the mass flow rate and the density. In the simulations the GVFA are no longer separated at the bottom of the tube and lies continuously in the inner curve at the tube. Large GVFA at the inlet and the outlet sections of the flowmeter are seen.

5.3 Assessment of Results

The simulations without oscillations give realistic results. The decoupling effect can be seen when comparing the measurement errors from the experiment and the observed increase of the GVFA, when the inlet GVF increases. The location of the GVFA fits well with known theories about pressure gradients in pipe bends.

The most important assumption in the simulations is the non oscillating domain since the simulations show GVFA which remains stationary in the flowmeter. The tube bend is in the x-y plane and the oscillations are in the y-z plane. The oscillations and fluid flow through the flowmeter creates Coriolis forces in the y-z plane. These forces could “move” the GVFA or “dissolve” these. So the most important question regarding the validity of the simulation results is:

- What effects will the oscillations have on the GVFA?

In Appendix H a rough estimation of the different forces effecting the bubbles in the Coriolis flowmeter is set up. The resulting forces in one bend of the flowmeter are crudely estimated to be 8 times smaller than the Coriolis force. The analysis showed that a few percentage of air in the fluid does not change the size of the forces acting on the fluid.

The pressure increases from the inner curve of the tube to the outer curve of the tube. The GVFA in the bend is created by the pressure gradient, since the bubbles moves toward lower pressure. Due to the size of the estimated Coriolis force compared to all the other forces acting on the fluid, the author would expect the oscillations to have an impact on the fluid behaviour in the flowmeter.

The error seen in the experiment when increasing the GVF is not only caused by the larger Coriolis force but more likely the decoupling effect.

Currently there is no adequate theory to explain the errors due to phase decoupling of two-phase fluids. The "bubble theory" is the best known theory at this point. It is a theoretical treatment of the errors due to phase decoupling. The "bubble theory" has several assumptions which makes it unrealistic, when analysing the simulation results. For example; is a constant volumetric particle fraction assumed along with assuming no pressure loss between the inlet and outlet of the flowmeter. Here a particle can be either a solid or a fluid (gas bubble or liquid droplet). [Basse, 2014a]

The described estimation procedure for GVF in Section 2.3 is one way to indicate the size of errors in measurement and the GVF. Another possible way could be a digital Coriolis transmitter, which can operate with highly aerated fluids, which is suggested in the paper by [Liu et al., 2001]. The transmitter correct the measurements based entirely on internally observed parameters and keeps the measurement error to a tenth of the existing error. The corrections are based on experimental data sets which are obtained at an experimental setup similar to the one used to gather the data used in Chapter 3. [Liu et al., 2001] observes that the "bubble theory"[1] only follows the general trend in how the mass flow error varies with low flow rates (<1.5 kg/s) and that a more detailed model is needed.

No commercial flowmeter exist at this point that can handle two-phase flow with the same level of accuracy as the single-phase flow.

[1]Note that this theory has later been reviewed several times, see for example [Basse, 2014a]

Chapter 6

Conclusion

The main goal for this project has been to investigate the influence of aerated flow in a Coriolis flowmeter. Theories applied for two-phase flow are the knowledge base from which experiments are performed and the measurement errors from two different Coriolis flowmeters are quantified. Computational Fluid Dynamic, CFD simulations of two-phase flow show the fluid behaviour in a SITRANS FC400 sensor for a Coriolis flowmeter.

The theory of two-phase flow are based on flow regimes in horizontal and vertical pipes. The Weisman model gives a set of equations to identify the flow regime in a horizontal pipe. The Mandhane flow regime map identifies the flow regime based on the superficial velocities of the two-phases in the pipe.

The patent by [Bierweiler et al., 2010] proposes a theory to estimate the GVF with the use of inverse envelopes, standard deviation of the phase shift and frequency. The theory requires no further change of geometry or simulations of the Coriolis flowmeter. In order to implement this estimation, further testing is required to create the envelopes needed and the electronic hardware and software needed to perform the calculations.

Two different flowmeters have been tested on an Aerated flow test rig provided by Siemens A/S, Flow Instruments (Nordborg, Denmark). During the tests the back-pressure, the air and liquid flow rate are changed. The fluid mass flow rate, fluid density and drive level are measured by the Coriolis flowmeter. The measurement errors are quantified by comparing the measured data to measurements performed with a second reference Coriolis flowmeter.

The measurements show an increase in fluid mass flow rate and fluid density errors, when the GVF and the liquid flow rate are increased. The drive level measured for Meter 2 shows an increase in the power level to vibrate the tubes, as both the GVF and the liquid flow rate increases. The average fluid mass flow error and fluid density error below a GVF of 5% meets the NAMUR 132 recommendations. Above 5% GVF the errors increase significantly.

A CFD simulation is set up based on a mesh, which is design after ERCOFTAC's "best practices guidelines". A grid convergence study is performed with the Grid Convergence Index which is based on Richardson's Extrapolation.

A mixture model, k-ω turbulence model simulation is performed for different cases. A steady and transient single-phase case are examined in order to find an acceptable initial solution and see general fluid behaviour.

Recirculation zones in the flowsplitters are first noticed when performing the single-phase simulations. Transient two-phase simulations shows high gas volume fraction areas, GVFA in the tube. As the liquid flow rate or the GVF increases so does the size of the GVFA. The GVFA lies in the bends of the tube, where there is a pressure gradient caused by the fluid change of direction. The fluid change of direction creates small recirculation zones at the inner curve of the tube after the bend, which shift the core of the flow to the of outer curve of the tube after the bend.

The measurement errors seen with aerated flow is in agreement with the simulated flow behaviour in the Coriolis flowmeter and the theory of two-phase flow behaviour.

An assessment of the validity of the simulation results without oscillations are investigated by setting up the forces acting on the fluid in a bend in the tube. The estimated Coriolis force is at least eight times larger than any other forces acting on the fluid. There is no significant change to the size of the Coriolis force when the fluid is changed from pure water to a mixture with a 5% GVF. It can be concluded that the measurement errors seen in the experiments, when the GVF increases, is not caused by the larger Coriolis forces but by the decoupling effect.

Several recommendations are given in Chapter 7 regarding experiments and simulations. These should be seen as the next steps in improving the measurement accuracy for aerated flow measurements in a Coriolis flowmeter.

Chapter 7

Recommendations

During the process of writing this thesis several ideas for improvements and further focus of study have appeared. The recommendations are based on the area of this report as seen in Figure 1.9 in Section 1.2 and should be seen as the next step to continue the improvement and study of aerated flow in the Coriolis flowmeter. The recommendations will be described in the following sections.

Drive Level Influence on Accuracy

In the experiments it was possible for Meter 2 to measure the drive level. The drive level increased as the GVF and liquid flow rate increased. It was hypothesized that the measurement error experienced is connected to the maximum drive level and that a higher maximum drive level would decrease the measurement error. System changes to the Coriolis flowmeter are required in order to validate this hypothesis.

Oscillations of the Tubes in Simulations

The simulations performed has been in a steady solid structure, which means that no oscillations have been introduced. The oscillations could be introduced with a gravitation-component perpendicular to the flow direction. The oscillations would create Coriolis forces in the entire domain and thereby impact the flow. A rough estimation of the forces affecting the flow shows that the Coriolis force is several times larger than the other forces in play, see Section 5.3 and Appendix H. A model taking into account the oscillations is crucial to gain a better understanding and to achieve a trustworthy picture of the flow behaviour.

Simulation Settings

The results from the simulations have been found with the use of the mixture model and the k-ω turbulence model. Further study of the models and their impact is needed in order to see, to what extent the model choices have had an impact on the results.

Flow Regime Input in the Simulations

The simulations performed have been with a dispersed bubble flow at the inlet of the Coriolis flowmeter. The dispersed bubble flow is only one of several flow regimes. In order to simulate the fluid behaviour in the Coriolis flowmeter several simulations with varying flow regimes will need to be performed.

Insight into Flow Behaviour

The experiments give no clear insight into the flow behaviour in the flowmeter and the simulations gives only insight over a short period of time. A see-through transmitter, x-ray or Particle Image Velocimetry, PIV are methods to see the flow behaviour in the transmitter in a longer period of time. This insight could establish whether there is undesirable flow behaviour *e.g.* slug flow.

Geometry Influence

Changes to the geometry of the SITRANS Coriolis flowmeters are difficult due to design patenting. An analysis of the geometry has a high value since the geometry has a significant influence on the flow regime of aerated flow. The tubes sides of the FC400 sensor have a high angle which increases the chances of slug flow. The geometry of the flowsplitters could be a focus point since they create recirculation zones in both the single and two-phase fluid case. This can be seen from the CFD simulations performed in Section 5.2.

The Dean number, mentioned in Chapter 3, suggest that increasing the curvature radius would improve the measurement accuracy. A higher curve radius could change the GVFA location and size in the flowmeter and thereby the effect of the decoupling.

References

Ali, Doolan, and Wheatley, **December 2009**. Mohamed Sukri Mat Ali, Con J. Doolan, and Vincent Wheatley. *Grid convergence study for a two-dimensional simulation of flow around a square cylinder at a low reynolds number.* Seventh International Conference on CFD in the Minerals and Process Industies, CSIRO, Melbourne, Australia, 2009.

ANSYS, Inc., **September 2006**. ANSYS, Inc. *ANSYS FLUENT User's Guide*, 6.3 edition, 2006.

ANSYS, Inc., **October 2012**. ANSYS, Inc. *ANSYS FLUENT Meshing User Guide*, 14.5 edition, 2012.

ANSYS, Inc., **November 2010**. ANSYS, Inc. *ANSYS CFX-Solver Modeling Guide*, 13.0 edition, 2010.

ANSYS, Inc., **November 2011**. ANSYS, Inc. *ANSYS FLUENT Theory Guide*, 14.0 edition, 2011.

Awad, **2012**. M.M. Awad. *Two-phase flow, chapter 11 from An Overview of Heat Transfer Phenomena.* ISBN 978-953-51-0827-6, 2012.

Basse, **April 2014a**. Nils Tångefjord Basse. *A review of the theory of Coriolis flowmeflow measurement error due to entrained particles.* Flow Measurement and Instrumentation, 37, 107–118, 2014.

Basse, **Januar-May 2014b**. Nils Tångefjord Basse. *Personal communications.* 2014. Siemens A/S, Flow Instruments.

Bierweiler, **Januar-March 2014**. Thomas Bierweiler. *Personal communications.* 2014. Siemens A/S, Flow Instruments.

Bierweiler, Ens, and Lenz, **2010**. Thomas Bierweiler, Eolfgang Ens, and Henning Lenz. *Coriolis mass flow meter and method for operating a coriolis mass flow meter*, 2010. Patent number: EP2297552B1.

Brennen, **2005**. Christopher E. Brennen. *Fundamentals of Multiphase Flows.* Cambridge University Press, 2005. ISBN 0521 848040. California Institute of Technology.

Celik, 2003. Ismail B. Celik. *Procedure for Estimation and Reporting of Discretization Error in CFD Applications*. 2003. Mechanical and Aerospace Engineering Department, West virginia University.

Christensen, Giversen, Thomassen, Andreasen, and Juhl, 2012. Mads Smed Christensen, Mike Dahl Giversen, Peter Hedegaard Thomassen, Morten Lind Andreasen, and Katrine Arnoldsen Juhl. *Free Jet Entrainment in Steady Fluid*, AAU, 2012.

Daniel L. Gysling, April 2007. Daniel L. Gysling. *An aeroelastic model of Coriolis mass and density meters operating on aerated mixtures*. Flow Measurement and Instrumentation, 18(2), 69–77, 2007.

ERCOFTAC, January 2000. ERCOFTAC. *Best Practice Guidelines*. Special Interest Group on "Quality and Trust in Industrial CFD, European Research Community On Flow, Turbulence and Combustion, 2000. ERCOFTAC.

Liu, Fuent, Henry, and Duta, March 2001. R.P. Liu, M.J. Fuent, M.P. Henry, and M.D. Duta. *A neutral network to correct mass flow error caused by two-phase flow in a digital coriolis mass flowmeter*. Flow Measurement and Instrumentation, 12(1), 53–63, 2001. doi: http://dx.doi.org/10.1016/S0955-5986(00)00045-5.

Lund and Condra, August 2013. Erik Lund and Thomas J. Condra. *Notes and exercises for numerical methods*. Aalborg University, 2013.

Mandhane, Gregory, and Aziz, 1974. J.M. Mandhane, G.A. Gregory, and K. Aziz. *A flow pattern map for gas-liquid flow in horizontal pipes*. International Journal of Multiphase flow, 1, 537–553, 1974.

Munson, Young, Okiishi, and Huebsch, 2010. Bruce R. Munson, Donald F. Young, Theodore H. Okiishi, and Wade W. Huebsch. *Fundamentals of Fluid Mechanics*. Wiley, ISBN: 978-0470-39881-4, 6 edition, 2010.

NAMUR Recommendation, 05 2009. NAMUR Recommendation. *Coriolis Mass Meter (CMM) NE 132*. NAMUR, 2009.

Siemens A/S, Flow Instruments, 2012. Siemens A/S, Flow Instruments. *SITRANS FC430 with HART, Operating Instructions*, 06 edition, 2012.

Siemens A/S, Flow Instruments, Maj 2014. Siemens A/S, Flow Instruments. *Picture of FC430*, 2014. Access 6 May 2014.

Siemens A/S, Flow Instruments 01 News, 2012. Siemens A/S, Flow Instruments 01 News. *Datasheet for Flow sensor SITRANS FCS400*. SIEMENS A/S, 2012.

Slater, July 2008. John W. Slater. *Examining Spatial (Grid) Convergence*. NPARC Alliance CFD Verification and Validation Web Site., 2008. Access 26 April 2014.

Time, 2009. Rune W. Time. *Two-phase flow in pipelines*. Department of Petroleum Engineering. Faculty of Science and Technology, University of Stavanger, 2009. Course compendium.

University of Massachusetts Lowell, **April 2014**. University of Massachusetts Lowell. *Natural Frequencies for Common Systems*. IES Seminar, 2014. Modal Analysis and Controls Laboratory. Access 26 April 2014.

Weinstein, **2008**. Joel Aaron Weinstein. *The motion of bubbles and particles in oscillating liquids with applications to multiphase flow in coriolis meters*. University of Colorado. PhD thesis, 2008. ISBN: 9780549672616.